Atmospheric Oxidation in the Presence of Clouds during the Deep Convective Clouds and Chemistry (DC3) Study

William H. Brune[1], Xinrong Ren[2,3], Li Zhang[1], Jinqiu Mao[4], David O. Miller[1], Bruce E. Anderson[5], Donald R. Blake[6], Ronald C. Cohen[7], Glenn S. Diskin[5], Samuel R. Hall[8], Thomas F. Hanisco[9], L. Gregory Huey[10], Benjamin A. Nault[11,*], Jeff Peischl[12,13], Ilana Pollack[12,13,#], Thomas B. Ryerson[13], Taylor Shingler[14,15], Armin Sorooshian[16,17], Kirk Ullmann[8], Armin Wisthaler[18], and Paul J. Wooldridge[7]

[1]Department of Meteorology and Atmospheric Science, Pennsylvania State University, University Park, PA
[2]Department of Atmospheric and Oceanic Science, University of Maryland, College Park, MD
[3]Air Resources Laboratory, National Oceanic and Atmospheric Administration, College Park, MD
[4]Department of Chemistry and Biochemistry, University of Alaska, Fairbanks, Fairbanks, AK
[5]Chemistry and Dynamics Branch, NASA Langley Research Center, Hampton, VA
[6]Department of Chemistry, University of California, Irvine, CA
[7]Departments of Chemistry and Earth and Planetary Sciences, University of California, Berkeley, Berkeley, CA
[8]Atmospheric Chemistry Observations and Modeling Laboratory, National Center for Atmospheric Research, Boulder, CO
[9]Atmospheric Chemistry and Dynamics Branch, Goddard Space Flight Center, Greenbelt, MD
[10]School of Earth and Atmospheric Sciences, Georgia Institute of Technology, Atlanta, GA
[11]Department of Earth and Planetary Sciences, University of California, Berkeley, Berkeley, CA
[12]Cooperative Institute for Research in Environmental Sciences, University of Colorado, Boulder, CO
[13]Earth System Research Laboratory, National Oceanic and Atmospheric Administration, Boulder, CO
[14]Science Systems and Applications, Inc., Hampton, VA
[15]Atmospheric Composition Branch, NASA Langley Research Center, Hampton, VA
[16]Department of Chemical and Environmental Engineering, University of Arizona, Tucson, AZ
[17]Department of Hydrology and Atmospheric Sciences, University of Arizona, Tucson, AZ
[18]Department of Chemistry, University of Oslo, Oslo, Norway
* now at Cooperative Institute for Research in Environmental Sciences, University of Colorado, Boulder, CO
# now at Department of Atmospheric Science, Colorado State University, Ft. Collins, CO

Correspondence to: William H. Brune (whb2@psu.edu)

Abstract. Deep convective clouds are critically important to the distribution of atmospheric constituents throughout the troposphere but are difficult environments to study. The Deep Convective Clouds and Chemistry (DC3) study provided the environment, platforms, and instrumentation to test oxidation chemistry around deep convective clouds and their impacts downwind. Measurements on the NASA DC-8 aircraft included those of the radicals hydroxyl (OH) and hydroperoxyl (HO_2), OH reactivity, and more than 100 other chemical species and atmospheric properties. OH, HO_2, and OH reactivity were compared to photochemical models, some with and some without simplified heterogeneous chemistry, to test the understanding of atmospheric oxidation as encoded in the model. In general, the agreement between the observed and modeled OH, HO_2, and OH reactivity were within the combined uncertainties for the model without heterogeneous chemistry and the model including heterogeneous chemistry with small OH and HO_2 uptake consistent with laboratory studies. This agreement is generally independent of the altitude, ozone photolysis rate, nitric oxide and ozone abundances, modeled OH reactivity, and

aerosol and ice surface area. For a sunrise to midday flight downwind of a nighttime mesoscale convective system, the observed ozone increase is consistent with the calculated ozone production rate. Even with some observed-to-modeled discrepancies, these results provide evidence that a current measurement-constrained photochemical model can simulate observed atmospheric oxidation processes to within combined uncertainties, even around convective clouds. For this DC3 study, reduction in the combined uncertainties would be needed to confidently unmask errors or omissions in the model chemical mechanism.

1 Introduction

Deep convective clouds alter the chemical composition of the middle and upper troposphere (Chatfield and Crutzen, 1984). At its base, a cloud ingests air containing volatile organic compounds (VOCs) and anthropogenic pollutants emitted into the atmospheric boundary layer, lifts it to the upper troposphere where it spreads into the anvil and is eventually mixed with the surrounding air, including some from the lower stratosphere. Inside the convective cloud, the chemical composition is transformed: boundary layer air is diluted with cleaner mid-latitude air; water soluble chemical species are scrubbed by contact with cloud particles; and nitrogen oxides are added by lightning. At the same time, shading in the cloud core extends the lifetime of certain photochemically active compounds. This transformed chemical composition profoundly alters the atmospheric oxidation in the upper troposphere.

Atmospheric oxidation is driven primarily by hydroxyl (OH), whose concentration is strongly dependent on ozone (O_3), especially in the upper troposphere (Logan et al., 1981). Ozone is a source of OH through its destruction by solar ultraviolet radiation, which produces an excited state oxygen atom that can react with water vapor to produce OH. Hydroxyl reactions with methane (CH_4) and VOCs produce oxygenated volatile organic compounds (OVOCs), including organic peroxyl (RO_2, where $R = CH_3$, C_2H_5, …) and hydroperoxyl (HO_2). At the same time, OH reacts with carbon monoxide to produce HO_2. The reaction of these peroxyls with NO creates new nitrogen dioxide (NO_2), which then absorbs solar radiation to produce NO and $O(^3P)$, and $O(^3P)$ combines with O_2 to form new O_3. In the absence of nitrogen oxides ($NO_x = NO+NO_2$), the formation of OH and HO_2 acts to destroy ozone through OH production and the reactions O_3+HO_2 and O_3+OH. Thus, atmospheric oxidation is strongly dependent on the chemical composition of the air exiting deep convective clouds.

Deep convective clouds transform the chemical composition of the upper troposphere in several ways (Barth et al., 2015, and references therein). NO_x produced by lightning can have mixing ratios of several parts per billion (ppbv) in the anvil downwind of convection (Ridley et al., 1996; Schumann & Huntrieser, 2007; Pollack et al., 2016; Nault et al., 2017). In addition to long-lived chemical species such CH_4, carbon monoxide (CO), and alkanes, short-lived chemical species such as isoprene and its reaction products or those found in fire plumes can be rapidly transported from the planetary boundary layer (PBL) by

convection into the upper troposphere (Apel et al., 2012; Apel et al., 2015). Convection also provides cloud particle liquid and solid surfaces, which can interact with gas-phase chemical species such as peroxides, potentially scrubbing some chemical species from the gas-phase, thereby altering the gas-phase chemistry and its products (Jacob, 2000; Barth et al., 2016). The mixture of organics and nitrogen oxides forms organic nitrates, which act as sinks for both organic and hydrogen radicals and nitrogen oxides (Nault et al., 2016). This mixture of organic and hydrogen peroxyl and nitrogen oxides is calculated to enhance upper tropospheric O_3 production in the range of a 2-15 ppbv day^{-1} (Pickering et al., 1990; Ren et al., 2008; Apel et al., 2012; Olson et al., 2012). Much of upper tropospheric OH and HO_2 is produced by the photolysis of oxygenated chemical species such as formaldehyde (CH_2O) and peroxides, which are products of organic chemical species that were lofted into the upper troposphere (Jaeglé et al., 1997; Wennberg et al., 1998; Ren et al., 2008).

Aircraft observations of tropospheric OH and HO_2 have been compared to photochemical box models constrained by other simultaneous measurements (Stone et al., 2012). In the planetary boundary layer, measurements of HO_2 (Fuchs et al., 2011) and, in some instruments, measurements of OH (Mao et al., 2012) are affected by interferences due predominantly to high abundances of alkenes and aromatics. In the free troposphere where the abundances of these chemical species are much lower, measured and modeled OH and/or HO_2 often agreed to within their combined uncertainties, which are similar to those for ground-based studies (Chen et al., 2012; Christian et al., 2017), but in most of these studies, either modeled and measured OH or HO_2 inexplicably disagreed beyond combined model and measurement uncertainty for certain altitudes or chemical compositions (Mauldin et al., 1998; Faloona et al., 2000; Tan et al., 2001; Olson et al., 2004; Olson et al., 2006; Ren et al., 2008; Stone et al., 2010; Kubistin et al., 2010; Olson et al., 2012; Regelin et al., 2013).

Only a few studies included OH and HO_2 measurements to test the impact of deep convective clouds on atmospheric oxidation in the upper troposphere. During the First Aerosol Characterization Experiment (ACE-1), modeled OH was 40% greater than measured OH in clouds, possibly due to uptake of OH or HO_2 on the cloud particles (Mauldin et al., 1998). In a different study, downwind of persistent deep convective clouds over the United States, the ratio of measured-to-modeled HO_2 increased from approximately 1 below 8 km altitude to 3 at 11 km altitude, suggesting an unknown source of HO_x (= OH+HO_2) coming from the nearby convection (Ren et al., 2008). During the African Monsoon Multidisciplinary Analyses (AMMA) campaign, daytime HO_2 observations were generally simulated with a photochemical steady-state model, but not in clouds, where modeled HO_2 greatly exceeded observed HO_2 (Commane et al.,2010), suggesting HO_2 uptake on liquid cloud drops.

Heterogeneous chemistry on aerosol can impact OH and HO_2 abundances (Burkholder et al., 2015 and references therein). Typical OH and HO_2 accommodation coefficients used in global models are 0.2 on aerosol particles and 0.4-1.0 on ice. Results from a study over the north Atlantic Ocean indicated that the lower observed-than-modeled HO_2 could be resolved by including heterogeneous HO_2 loss (Jaeglé et al., 2000), but this did not resolve the same difference in clear air. This result differs from an analysis of in-cloud measurements over the western Pacific, which provide evidence that uptake in ice clouds has little

impact on HO_2 (Olson et al., 2004). However in the same study, the observed-to-modeled HO_2 during liquid cloud penetrations was on average only 0.65, compared to 0.83 outside of clouds, and this difference depended upon both the duration of the cloud penetration and the liquid water content (Olson et al., 2006). The uptake of HO_2 in liquid cloud particles was also observed by Whalley et al. (2015).

Laboratory studies show that the HO_2 effective uptake coefficient on moist aerosol particles that contain copper is probably much less than 0.01 in the lower troposphere but may be greater than 0.1 in the upper troposphere (Thornton et al., 2008). However, other laboratory studies show that adding organics to the particles or lowering the relative humidity can reduce uptake coefficients (Lakey et al., 2015; Lakey et al., 2016). These values are generally lower than the HO_2 effective uptake coefficient assumed in global chemical transport models. On ice surfaces, the OH uptake coefficient is thought to be at least 0.1 and probably larger (Burkholder et al., 2016). In global models, metal catalyzed HO_2 destruction on aerosol particles can reduce global HO_2 in a way that is more consistent with observed OH and HO_2 (Mao et al., 2010). More recently, a global sensitivity analysis shows that modeled HO_2 is most sensitive to aerosol uptake at high latitudes (Christian et al. 2016), consistent with the conclusion of Mao et al. (2010).

In this paper, we focus on the comparison of measured and modeled OH and HO_2 near deep convective clouds and the implications of this comparison. Our goal is to test the understanding of atmospheric oxidation around deep convective clouds and in the cloud anvils. One possible effect is heterogeneous uptake of OH, HO_2, and RO_2 around and in these clouds, which could alter OH and HO_2. The data for this analysis were collected during the Deep Convective Clouds and Chemistry (DC3) study in 2012.

2 Measurement and modelling methods

2.1 The DC3 Study

Barth et al. (2015) provide a detailed description of the objectives, strategy, locations, instrument payloads, and modeling for DC3. DC3 was designed to quantify the link between the properties of deep convective clouds and changes in chemical composition in the troposphere. This section provides information on the aspects of DC3 that relate most directly to the measured and modeled OH, HO_2, and OH reactivity.

DC3 involved several heavily instrumented aircraft, ground-based dual Doppler radar, lightning mapping arrays, and satellites (Barth et al., 2015). Studies were generally focused on areas in Colorado, Texas/Oklahoma, and Alabama that had dual Doppler radar coverage to quantify cloud properties. The field study took place in May through June, 2012. The aircraft were based in Salina, Kansas, which was central to the three main target regions in Colorado, Texas/Oklahoma, and Alabama. The NASA DC-8 sampled deep convection six times in Colorado, four times in Texas/Oklahoma, and three times in Alabama. Typically

working with the NSF G-V aircraft, the DC-8 would sample the inflow region to a growing cumulus cloud and then after it formed, spiral up to the anvil height (~8-12 km) and join the NSF G-V in sampling the outflow region of the same convection.

In addition, during the night before 21 June, the outflow from a mesoscale convective system (MCS) in the Midwest spread over Iowa and Missouri and then into Illinois and Tennessee. The DC-8 sampled the outflow of this MCS starting at sunrise of 21 June, flying six legs, each approximately 400 km long, across the outflow roughly perpendicular to the wind and adjusting the downwind distance to account for the outflow velocity (Nault et al., 2016). The southern 2/3 of the first three legs was in a thin cirrus cloud and the rest was clear.

Most DC3 flights began late morning in order to be in position to sample near active deep convection occurring in late afternoon and concluded near dusk for safety. About 90% of the flight time occurred when the solar zenith angle was less than 85°. Only the photochemical evolution flight on 21 June began before dawn.

The NASA DC-8 aircraft was the only aircraft that had an instrument to measure OH and HO_2. The DC-8 payload was quite comprehensive, thus providing detailed chemical composition, particle characteristics, and meteorological parameters to constrain the photochemical box model that is used to compare observed and modeled OH and HO_2. Direct comparison between observed and modeled OH and HO_2 is valid because the lifetimes of OH and HO_2 are short, a few seconds or less for OH and a few 10's of seconds for HO_2. Thus, the analyses in this paper uses only measurements from the DC-8.

2.2 Measurement of Hydroxyl (OH) and Hydroperoxyl (HO_2)

OH and HO_2 were measured with the Penn State Airborne Tropospheric Hydrogen Oxides Sensor (ATHOS), which uses laser induced fluorescence (LIF) in low pressure detection cells (Hard et al., 1984). ATHOS is described by Faloona et al. (2004). Sampled air is pulled through a 1.5 mm pinhole into a tube that leads to two detection axes. The pressure varies from 12 hPa at low altitudes to 3 hPa aloft. The laser beam is passed 32 times through the detection region with a multipass cell set at right angles to the gated microchannel plate detector. As the air passes through a laser beam, OH absorbs the laser radiation (3 kHz repetition rate, 20 ns pulse length) and fluoresces. In the first 100 ns, the signal contains fluorescence as well as scattering from the walls, Rayleigh scattering, and clouds drops. OH fluorescence is detected from 150 ns to 700 ns after each laser pulse. OH is detected in the first axis; reagent nitric oxide (NO) is added before the second axis to convert HO_2 to OH, which is then detected by LIF. The laser wavelength is tuned on-resonance with an OH transition for 15 seconds and off-resonance for 5 seconds, resulting in a measurement time resolution of 20 seconds. The OH fluorescence signal is the difference between on-resonance and off-resonance signals. The ATHOS nacelle inlet is attached below a nadir plate of the forward cargo bay of the DC-8 and the lasers, electronics, and vacuum pumps were inside the forward cargo bay.

In clouds, cloud particles can be pulled into the detection system and remain intact enough to cause large, short scattering signals in the fluorescence channels randomly during on-resonance and off-resonance periods. Differencing these signals to find OH creates large positive and negative noise, which reduces the measurement precision by as much as a factor of five. When the background signal due to these cloud particles exceeded the average background signal by four standard deviations, the on-line and off-line data were removed from the data set before the analyses were performed. Less than 3% of the data were removed. The overall results for OH and HO_2 vary less than 4% for filtering between two and six standard deviations.

The instrument was calibrated on the ground both in the laboratory and during the field campaign. Different sizes of pinholes were used in the calibration to produce different detection cell pressures to mimic different altitudes. Monitoring laser power, Rayleigh scattering, and laser linewidth maintained this calibration in flight. For the calibration, OH and HO_2 were produced through water vapor photolysis by UV light at 184.9 nm. Absolute OH and HO_2 mixing ratios were calculated by knowing the 184.9 nm photon flux, which was determined with a Cs-I phototube referenced to a NIST-calibrated photomultiplier tube, the H_2O absorption cross section, the H_2O mixing ratio, and the exposure time of the H_2O to the 184.9 nm light. The absolute uncertainty was estimated to be ±16% for both OH and HO_2 at a 1σ confidence level. The 1σ precision for a one-minute integration time during this campaign was about 0.01 parts per trillion by volume (pptv, equivalent to pmol mol^{-1}) for OH and 0.1 pptv for HO_2. Further details about the calibration process may be found in Faloona et al. (2004).

For environments with substantial amounts of alkenes and aromatics, ATHOS has interferences for both OH (Mao et al., 2012) and HO_2 (Fuchs et al., 2011). New ATHOS measurement strategies have minimized these interferences, but these strategies were not fully developed in time for DC3. However, recent missions have shown that the OH interference is significant only just above forests or cities and is negligible above the PBL. On the other hand, the deep convective clouds encountered in DC3 can lift short-lived VOCs that cause the HO_2 interference to the upper troposphere. Because the ATHOS was still sensitive to this RO_2 interference in DC3, we are not able to determine if this interference is affecting the HO_2 observations around and in these clouds. For OH, we will factor in the likelihood that the OH has an interference in the PBL above forests in the discussion comparing observed and modeled OH.

For HO_2, the correction method uses more than 1000 RO_2 chemical species modeled by MCMv3.3.1 and assumes that they are ingested into the detection flow tube without any wall loss. The model then calculates the resulting OH, which is what would be detected as HO_2. The calculated concentration of reactant NO is ~3×10^{13} cm^{-3} and the reaction time was determined to be 3.7 ms, as verified by the HO_2 conversion rate measured in the laboratory. This calculation was repeated for each one-minute time step and this calculated interference was then subtracted from the observed HO_2, resulting in the HO_2 values reported here. Observed HO_2 was reduced by an average of 2%, with some peaks of 10%, both in the PBL and aloft. Because the model RO_2 mechanisms are uncertain, the uncertainty for this correction is estimated to be a factor of 2, which increases the absolute uncertainty for HO_2 from ±16% to ±20%, 1σ confidence.

2.3 Measurement of OH Reactivity

The OH reactivity is the sum of the product of OH reactants and their reaction rate coefficients with OH and is the inverse of the OH lifetime. It is directly measured by adding OH to the air flowing through a tube and then monitoring the decay of the logarithm of the OH signal as the reaction time between the OH addition and OH detection is increased (Kovacs and Brune, 2001). OH can also be lost to the tube walls, so the measured OH reactivity must be corrected for this wall loss. The OH reactivity can be determined from the equation

$$k_{OH} = -\frac{ln\left([OH]/[OH]_0\right)}{\Delta t} - k_{wall} \tag{1}$$

where *[OH]₀* is the initial OH concentration, *[OH]* is the [OH] concentration after a reaction time Δt between OH and its reactants, and k_{wall} is the OH wall loss.

The OH reactivity is measured with the OH Reactivity instrument (OHR), which sits in a rack in the DC-8 forward cargo (Mao et al., 2009). Ambient air is forced into a flow tube (10 cm dia.) at a velocity of 0.3-0.7 m s^{-1}, flows past the pinhole of an OH detection system similar to the one used for ATHOS, and then is expelled out of the aircraft. In a movable wand in the center of the flow tube, OH is produced by the photolysis of water vapor by 185 nm radiation and then injected into the flow tube, mixing with the ambient air flow. As the wand is pulled back, the distance between the injected OH and the OH reactants in the air increases, resulting in the OH decay. The distance divided by the measured velocity gives the reaction time. The wand moves 10 cm in 12 s and then returns to the starting position, measuring a decay every 20 s.

The OHR calibration was checked in the laboratory before and after DC3 using several different known amounts of different chemical species. During a semi-formal OHR Intercomparison in Juelich Germany in October 2015, the OHR instrument was combined with a different laser, wand drive, and electronics, and despite the difficulties encountered, it was found to produce accurate OH reactivity measurements (Fuchs et al., 2017).

The uncertainty in the OH reactivity measurement consists of an absolute uncertainty and the uncertainty associated with the wall loss subtraction. Changes in the OHR instrument between ARCTAS and DC3 result in slightly different instrument operation, wall loss, and measurement uncertainties between this paper and Mao et al. (2009). The pressure dependence of the OH wall loss was measured in the laboratory using ultra zero air (99.999% pure) and was found to between 2 s^{-1} and 4 s^{-1} over the range pressures equivalent to 0 to 12 km altitude. The flow tube wall is untreated aluminium so that every OH collision with the wall results in complete OH loss no matter the environment or altitude. Mao et al. (2009) confirm the zero found in the laboratory agrees with the zero found in flight. From these laboratory calibrations, the estimated uncertainty in the wall

loss correction is ± 0.5 s^{-1} (1σ confidence). When the OH reactivity is 1 s^{-1}, the combined uncertainty from the absolute uncertainty and the zero decay is ± 0.6 s^{-1}, 1σ confidence, which suggests that 90% of the measurements should be within ± 1.2 s^{-1} of the mean value.

5 Air entering the OHR flow tube was warmed by ~5°C at altitudes below 2 km to by as much as 75°C at 12 km. The flow tube pressure was 50 hPa greater than ambient due to the ram force pushing air through the flow tube. These temperature and pressure differences can affect the reaction rate coefficients for some OH reactants and thus change the OH reactivity. In order to compare observed and model-calculated OH reactivity, the model was run for both ambient conditions and for the OHR flow tube pressure and temperature, but the observed and model-calculated OH reactivity will be compared for the OHR flow 10 tube pressure and temperature.

2.4 Measurement of other chemical species, photolysis frequencies, and other environmental variables

Accurate measurements of other chemical species and environmental variables are critical for this comparison of measured and modeled OH, HO$_2$, and OH reactivity. The photolysis frequency measurements are particularly critical for DC3 because of all the time spent flying around clouds and in the deep convection anvil. A list of these measurements is given in Table S1 15 and is summarized in Barth et al. (2015; 2016) and Pollack et al. (2016). The list of measured chemical species includes CO, CH$_4$, N$_2$O, NO, NO$_2$, O$_3$, organic nitrates, alkanes, alkenes, aromatics, aldehydes, alcohols, and peroxides.

2.5 Photochemical Box Model

The photochemical box model used in this study is based on the Matlab-based modeling framework, the Framework for Zero-Dimensional Atmospheric Modeling (F0AM), which was developed and made freely available by Glenn Wolfe (Wolfe et al., 20 2016). The gas-phase photochemical mechanism was Master Chemical Mechanism v3.3.1 (MCMv331) (Saunders et al., 2003; Jenkin et al., 2003). This model was constrained by all simultaneous measurements of chemical species, photolysis frequencies, and meteorological variables (Table 1) and then run to calculate OH, HO$_2$, and all reaction products that were not measured, such as organic peroxy radicals. Pernitric acid (HO$_2$NO$_2$) was measured but was not used to constrain the model because few measurements were reported below 4 km. Measured and modeled HO$_2$NO$_2$ agree to within ~25% from 5 to 9 km, and modeled 25 HO$_2$NO$_2$ is 1.7 times that measured above 8 km. This difference between using modeled and observed HO$_2$NO$_2$ made only a few percent difference in modeled OH and HO$_2$.

A publically available merge file provided the constraining measurements for the photochemical model (DC3 Data, 2017). We chose the one-minute merge as a compromise between higher frequency measurements that needed to be averaged into one-30 minute bins and lower frequency measurements that needed to be interpolated between one-minute bins. OH and HO$_2$ measurements, made every 20 seconds, were averaged into the one-minute bins.

Heterogeneous chemistry was added to the model for some model runs. While many chemical species undergo heterogeneous chemistry, most of the chemical species that strongly influence OH and HO_2 were measured so that their heterogeneous chemistry can be ignored in these comparisons between observed and modeled OH and HO_2. However, organic peroxyl radicals were not measured and their heterogeneous chemistry could have an influence on OH and HO_2. Thus, heterogeneous
5   chemistry is implemented in the model for OH, HO_2, and RO_2, even though the uptake of RO_2 is thought to be small.

The common types of particles encountered with convection are humidified sub-micron aerosol particles all around and in the convection, liquid drops in lower altitude clouds, and ice particles in the deep convective cloud anvil. The effective uptake of OH, HO_2, and RO_2 onto these surfaces was found from

$$\frac{1}{\gamma_{eff}} = \left(\gamma_{surface} + \left(\frac{1}{\alpha} + \frac{1}{\gamma_{sol} + \gamma_{rxn}}\right)^{-1}\right)^{-1} + \frac{0.75 + 0.286\, Kn}{Kn\,(Kn+1)} \qquad (2)$$

where γ_{eff} is the effective uptake coefficient, $\gamma_{surface}$ is surface reaction uptake, α is the accommodation coefficient, γ_{sol} is uptake due to diffusion through the liquid, γ_{rxn} is uptake due to aqueous-phase reactions, and the last term is the inverse of the gas-
15   phase diffusion in terms of the Knudsen number, Kn (Burkholder et al., 2016; Tang et al., 2014). The first term on the right-hand side is the total uptake coefficient, γ_{total}. The gas-phase molecular diffusion of chemical species to the particle surface can limit the uptake, especially for large accommodation coefficients and large particles.

The total uptake coefficient for OH and HO_2 depends on the particle chemical composition, phase, and size (Burkholder et al.,
20   2015). While some particle properties were measured in DC3, there are unknowns in particle composition and uncertainties in trying to calculate the uptake coefficient for each one-minute time step. The goal of including heterogeneous chemistry in the model is to determine if heterogeneous chemistry has a substantial impact on the comparison between the observed and modeled OH and HO_2. Thus, we will run the model with fixed values for the total uptake; if the impact on the modeled OH and HO_2 is substantial, then we will have to improve the parameterization of the total uptake.

For aerosol particles, the dry aerosol particle radius is multiplied by the growth factor and then the area-weighted median ambient aerosol radius is determined. The surface area is found by summing the surface area in each bin, multiplied by the bin width, and then corrected by the square of the growth factor for each minute. Ice particles are assumed to be spherical and their size distribution is used to determine the median particle radius. The surface area per cm^{-3} of air is determined by summing
30   the surface area per cm^{-3} of air times the bin width, which were provided in the merge file for each minute.

The model is then run for three primary different cases: gas-phase with no heterogeneous chemistry (called "no-het"), heterogeneous chemistry (called "het") with $\alpha_{aer} = 0.2$ (which is consistent with the value used in some global models) and α_{ice}

= 1.0 for OH, HO_2, and RO_2, and maximum heterogeneous chemistry (called "hetmax") with α_{aer} = 1.0 and α_{ice} = 1.0. The observed and modeled OH and HO_2 are compared for these three cases.

OH reactivity was also modeled for comparison to observed OH reactivity. Modeled OH reactivity was calculated from the measured chemical species plus OH reactants that were not measured but were produced by the photochemical model. Examples of these additional OH reactants are organic peroxy, organic peroxides, and unmeasured aldehydes. Uncertainty in the modeled OH reactivity is estimated to be $\pm 10\%$, 1σ confidence (Kovacs et al., 2001)

Uncertainty in the photochemical box model can be assessed with Monte Carlo methods in which model constraints are varied randomly over their uncertainty ranges and then the widths of the resulting distributions for OH and HO_2 abundances are used to determine the model uncertainties. If just reaction rate coefficients, photolysis frequencies, and reaction products are varied, the typical OH and HO_2 uncertainties at the 1σ confidence level are typically $\pm(10\text{-}15)\%$ (Thompson and Stewart, 1991; Kubiston et al., 2010; Olson et al., 2012; Regelin et al., 2013). When uncertainties in the measurements used to constrain the model are included, uncertainties at the 1σ confidence level are typically $\pm 20\%$ or more for both local and global models (Chen et al., 2012; Christian et al., 2016). We use $\pm 20\%$ uncertainty at the 1σ confidence level for the model uncertainty in this paper, which can be combined with the measurement uncertainty of about $\pm 20\%$ uncertainty at the 1σ confidence level. We note that the observed-to-modeled difference for statistical significance lies approximately at the sum of the standard deviations of the mean for the observations and model. As a result, the factors of 1.4 and 1/1.4 serve as indicators for agreement between observed and modeled OH, HO_2, and OH reactivity.

We decided to make the comparisons between observations for all the DC3 results, including transits from Salina KS to the deep convection regions. Using all the data gives a more robust comparison and was found to give comparison results identical to that using data sets restricted to the radar-enhanced sites in Colorado, Texas/Oklahoma, and Alabama near vicinity of convection. The direct impact of deep convection is also tested by examining the observed-to-modeled comparison as a function of the ice surface area per cm^{-3} of air. This analysis achieves the goals laid out in the introduction.

The model was run 27 times to test the sensitivity of the calculated OH and HO_2 to different factors. First, the chemical mechanism was expanded to include the reactions of CH_3O_2+OH and $C_2H_5O_2+OH$ (Assaf et al., 2017), and in some cases, reactions of OH with the next 300 most significant RO_2 species that comprise 95% of the modeled RO_2 total, assuming a reaction rate coefficient of $10^{-10}\,cm^{-3}s^{-1}$. Adding the measured reactions decreased OH by ~1% (5% maximum) and increased HO_2 by <1% (15% maximum); adding the assumed reactions of OH with other RO_2 species changed modeled OH and HO_2 by less than 3%. Second, the decay frequency of the unconstrained modeled oxygenated intermediates was varied from 6 hours to 5 days. The resulting modeled OH and HO_2 varied by ~10% over this range. This decay time serves as a proxy for surface deposition in the planetary boundary layer as well as for recently measured rapid reactions of highly oxidized $RO_2 + RO_2$ to

form peroxides (Bernt et al., 2018). This decay time is highly uncertain. The mean of the model runs using decay times of 6 hours, 1 day, and 5 days and using the model mechanism including CH_3O_2+OH and $C_2H_5O_2+OH$ was used for the comparisons to the measurements.

3 Results

5 The DC3 chemical environments dictate the OH and HO_2 abundances. Using all the flight data, altitude profiles of NO, CO, O_3, and particle surface area were collected into 0.5 km altitude bins and the median values were found (Fig. 1). The radar altitude is used for these comparisons because the surface elevations and thus planetary boundary layer (PBL) is at different pressure altitudes for the Colorado, Texas/Oklahoma, and Alabama regions.

10 Median NO exhibits a "C"-shaped profile with median values near 50 pptv in the planetary boundary layer, a minimum of 10 pptv at 5 km altitude, and a maximum value of 0.5 ppbv above 10 km. NO in the PBL was largely due to anthropogenic pollution; NO aloft was mainly due to a combination of lightning and stratospheric NO_x. Median CO slightly decreased from ~120 ppbv near the surface to ~80 ppbv at 12 km. Median O_3 was 50 ppbv in the PBL and then increased to as much as 100 ppbv near 12 km, likely due to stratospheric ozone influence. The surface area per cm^{-3} of air of aerosol was 10^{-6} cm^2cm^{-3} in

15 the PBL, but was about $3x10^{-7}$ cm^2cm^{-3} above that. Median ice surface area was as much as $2x10^{-5}$ cm^2cm^{-3}, with high variability spanning a factor of 100.

3.1 Comparing HO_x Observations with the no-het Model

Observations will be compared to the no-het model, which should be considered as the base case; the heterogeneous cases will be considered later. When observed and modelled OH and HO_2 are plotted against time, model results generally agree with

20 the observed values to within combined uncertainties, with occasional periods in which the observed values can be either much larger or smaller than all the model variants. A plot of this time series of observed and modeled OH and HO_2 includes fourteen model runs with model integration times varied from 3 to 24 hours, dilution frequencies varied from 6 hours to 5 days, and without or without including the RO_2+OH reaction (Fig. S1). Another way to examine these results is to plot the observed and modeled values as a function of altitude and other influential chemical species, photolysis frequency, or location.

Median observed OH was about $2x10^6$ cm^{-3} from ~3 km to 10 km altitude, but was greater than $3x10^6$ cm^{-3} below 3 km and just above 10 km, where a spike in OH brings the median OH to $3.5x10^6$ (Fig. 2). This profile is consistent with the NO profile; for the NO amounts measured in DC3, increased NO shifts more HO_x to OH. The median OH observed-to-modeled ratio for the no-het case is close to 1.0 at 0-4 km, is 1.2-1.3 between 5 km and 9 km and 0.8-0.9 above 10 km. Generally, the observed-

30 to-modeled ratio is within the estimated combined uncertainties described previously. The statistics from scatter plots using a fitting routine that considered uncertainty in both the observations and the model (York et al., 2004) indicate generally good agreement between observed and modeled OH, with the model explaining 85% of the OH variance (Table 2, Fig. S2).

Median observed HO_2 was 10-22 pptv below 2 km altitude and decreased almost linearly to 3 pptv at 12 km (Fig. 3). This profile is consistent the altitude distribution of HO_x sources, which are greater near the surface, and even with convective uplift of oxygenated chemical species such as HCHO, are still much less than at the surface. Again, the observed-to-modeled ratio is within the estimated combined uncertainties. In addition, the statistics from scatter plots indicate generally good agreement between observed and modeled HO_2, with the model explaining 68% of the HO_2 variance (Table 2, Fig. S2). However, the median observed-to-modeled ratio for the no-het case is 1.3 at 1 km altitude, decreases to ~1 at 5 km and remains near 1 above 5 km. The ratio of the modeled RO_2 to HO_2 is typically 1 in the PBL and 0.5 above 5 km. Error in our assumptions for the RO_2 interference in the HO_2 measurement is a possible cause of the greater observed-to-modeled HO_2 below 3 km, but this difference is still well within the combined uncertainty limits.

An indicator of the HO_x cycling between OH and HO_2 is the HO_2/OH ratio. If the primary HO_x production rate is smaller than the OH-HO_2 cycling rate and there is sufficient NO, the HO_2/OH ratio approximately equals the OH loss frequency that cycles OH into HO_2 divided by the reaction frequency of HO_2 reactions that cycle HO_2 to OH, primarily HO_2 reactions with NO and O_3. Both the observed and modelled HO_2/OH ratios are greater than 100 below 4 km and fall to less than 10 at 12 km (Fig. S3). This profile comes from the greater amount of OH reactants at lower altitudes, which increases the ratio, as opposed to the greater NO amount aloft, which decreases the HO_2/OH ratio. The observed-to-modeled ratio is within the approximate uncertainty limits (1σ confidence) of a factor of 1/1.4 to 1.4. .

Another good test of the model photochemistry is the comparison of observed and modeled OH and HO_2 as a function of controlling variables (Fig. 4). The photolysis frequency for O_3 producing an excited state O atom, $JO(^1D)$, and O_3 are both involved in the production of OH. O_3 and NO cycle HO_2 to OH, while modeled OH reactivity cycles OH back to HO_2. In general, measured and model OH and HO_2 agree from $2x10^{-6}$ s^{-1} to $7x10^{-5}$ s^{-1} for $JO(^1D)$, from $2x10^{-3}$ ppbv to $7x10^{-1}$ ppbv for NO, from 40 ppbv to 100 ppbv for O_3. For $JO(^1D)$ greater than $2x10^{-5}$ s^{-1}, the median observed-to-modeled HO_2 ratio is 0.98; the in-cloud ratio is an insignificant 10% less than in clear air, indicating that the observed photolysis frequency measurement is accurate even in clouds. The observed-to-modeled HO_2 ratio shows little evidence of a NO-dependence, although observed-to-modeled HO_2 exceeded 2 for ~2% of the values when NO was more than 0.5 ppbv. For the O_3 observations greater than 200 ppbv, which are 0.5% of all observations, the observed-to-modeled HO_2 and OH were both ~0.5. It is possible that the behavior as a function of controlling variables is also a function of altitude. However, with the exception of low values of $JO(^1D)$, the median observed-to-modeled OH and observed-to-modeled HO_2 are generally independent of both the controlling variables and altitude (Fig. S4). The observed-to-modeled OH and HO_2 are also independent of whether the measurements were made in Colorado, Texas/Oklahoma, or Alabama (Fig. S5), although the ratios for some altitudes vary widely due to fewer data points in the altitude medians.

3.2 Comparing OH Reactivity Observations with the no-het Model

The measured OH reactivity was typically 2 s^{-1} to 5 s^{-1} in the PBL but fell off to less than 1 s^{-1} at 12 km altitude (Fig. 5). Observed and modeled OH reactivity are in reasonable agreement when considered in the context of the typical limit-of-detection for OH reactivity (Fuchs et al., 2017). For DC3, limit-of-detection for 20-second measurements is estimated to be about 0.6 s^{-1}, which means that most OH reactivity measurements were at or below the limit-of-detection. The modeled OH reactivity for the OHR flow tube temperature and pressure is greater than the modeled OH reactivity for ambient temperature and pressure by about 0.3 s^{-1} below 2 km and by about 0.2 s^{-1} above 10 km (Fig. 5). This difference is negligible below 2 km, but grows to a factor of 1.7 at 10 km where the ambient OH reactivity is just 0.2-0.3 s^{-1}, but for the entire altitude, the difference between the observed and modeled OH reactivity is 0.2 s^{-1} larger for the modelled OH reactivity at OHR flow tube conditions than for the modelled OH reactivity at ambient conditions, a difference that is swamped by the noise in the observed OH reactivity. The median observed OH reactivity is 1-3 s^{-1} greater than the modeled OH reactivity below 3 km, and this difference could be evidence of missing OH reactivity.

The percent error between the OH reactivity calculated with modeled chemical species and that calculated from only the measured OH reactants is, on average, less than 4%. In the PBL over Alabama, the OH reactivity calculated from the model after one day of integration was on average 10% larger than that calculated from the chemical species measurements. In the Colorado and Texas PBL, the average difference was less than 4%. According to the model calculations, CO contributes the most to the OH reactivity, with ~20% in the PBL and 30-40% aloft. Next is CH$_4$ at (5-10)%, HCHO at (5-10)%, O$_3$ at (2-10)%, CH$_3$CHO at ~5%, and Isoprene at (1-2)%, except in some PBL plumes where it was as much as 60%. The most significant ten chemical species were all measured and account for (60-70)% of the total model-calculated OH reactivity. Thus, for much of DC3, the OH reactivity calculated from the DC3 measurements almost completely comprises the measured OH reactivity.

3.3 Comparing OH Production and OH Loss

Another critical test of OH photochemistry is the balance between OH production and loss (Fig. 6). The OH lifetime is typically tenths of a second or less in the PBL and a few seconds at high altitude. Thus, for one-minute averages, OH production and loss should essentially be in balance to within the uncertainty estimates from a propagation of error analysis. Modeled OH production and loss are in balance. These uncertainty estimates were obtained by assuming that OH production is dominated by HO$_2$+NO→OH+NO$_2$ and ozone photolysis followed by reaction of excited state oxygen atoms with water vapor and the OH loss is given by the OH reactivity multiplied by the OH concentration. The largest contributor to the uncertainty is the zero offset for the OH reactivity instrument. The observed OH loss is the observed OH multiplied by the observed OH reactivity, which was corrected for the difference between ambient and OHR flow tube conditions. While this analysis cannot preclude

missing or additional OH production and loss of 10^6 cm^{-3} s^{-1} or less, the OH production and loss, which are calculated mostly from observations, agree to within uncertainties.

3.4 Comparing HO$_x$ Observations with Models Containing Heterogeneous Chemistry

Ample aerosol and ice during DC3 provide tests for possible effects of heterogeneous chemistry on OH and HO$_2$. We look first at the impact that adding heterogeneous chemistry (het, $\alpha_{ice} = 1.0$; $\alpha_{aer} = 0.2$), and maximum heterogeneous chemistry (hetmax, $\alpha_{ice} = 1.0$; $\alpha_{aer} = 1.0$) to the model has on the comparison of median observed and modeled OH and HO$_2$.

In Figures 2-4 and S6-S7 and Tables 2 and S1, the no-het and het models agree with the observed OH and HO$_2$ to within the combined uncertainties, with the exception of the het model for HO$_2$ when the aerosol surface area per cm^{-3} of air was greater than 10^{-6} cm^2 cm^{-3}. In that case, the ratio of the observed-to-modeled HO$_2$ was too large, indicating that the het model was reducing HO$_2$ too much. On the other hand, the difference between the observations and hetmax model is greater than the uncertainty limits in almost every comparison. When the OH observed-to-modeled ratio is plotted as a function of aerosol surface area (Fig. 7), the no-het model gives a better agreement with the observations as a function of surface area than the het model does. For HO$_2$, the difference between the het model and the observations exceeds the combined uncertainty limits when the aerosol surface area per cm^{-3} of air exceeds 10^{-6} cm^{2}cm^{-3}.

For heterogeneous uptake on ice, the observed-to-modeled comparisons of OH and HO$_2$ are roughly independent of ice surface area (Fig. S8). Comparing the model with HO$_2$ uptake on ice equalling 1 to a model with HO$_2$ uptake on ice set to zero decreases OH and HO$_2$ by only 10% for the largest ice surface area per cm^{-3} of air of 7×10^{-5} cm^2 cm^{-3}. HO$_2$ uptake on ice causes at most a few percent decrease in HO$_2$.

The addition of RO$_2$ heterogeneous chemistry on aerosol and ice did reduce the modeled RO$_2$ by 10% on average for the het model, but did not reduce either OH or HO$_2$ by more than 1%, on average. Including RO$_2$ uptake along with OH and HO$_2$ uptake had only a small impact on the heterogeneous effects on OH and HO$_2$.

3.5 Evolution of OH and HO$_2$ Downwind of a Nighttime Mesoscale Convective System (MCS)

The quasi-Lagrangian tracking of convective outflow on 21 June provided an opportunity to test the photochemical evolution of OH and HO$_2$ in the morning of 21 June. The flight legs perpendicular to the wind were approximately advected downwind. Initially, observed and modeled OH and HO$_2$ were close to 0 (Fig. 8). However, both modeled OH and HO$_2$ soon grew to exceed measured OH and HO$_2$ by about 20%-50% until about 8 am local time. For the remainder of the flight, observed and modeled OH is in substantial agreement for all three models, which are essentially identical except between 9:30 and 11:00 when the aerosol surface area per cm^{-3} of air was the greatest. For HO$_2$, observed HO$_2$ exceeds modeled by a factor of ~1.5 after 9 (CST). In this time period, the observations agree best with the no-het and het models. Thus, the basic observed behavior

of OH and HO$_2$ is captured by the no-het and het models although there is quantitative disagreement between the model and observations of OH and HO$_2$ for local solar time between 5:45 and 8:15 (CST) and of HO$_2$ after 9 (CST).

Even though more than half of the first three legs were in an ice cloud, the scaled surface area for aerosol particles (Figure 8, top panel) and ice (Figure 8, bottom panel) do not correlate with the differences between observed and modeled OH and HO$_2$.

As a test of the photochemistry, OH can be calculated from the observed decay of OH reactants. Nault et al. (2016) showed that the observed decay of ethane, ethyne, and toluene were consistent with an average observed OH of 9.5x10^6 cm^{-3} for times from 7:35 to 9:50 local time. An ATHOS recalibration since the publication of Nault et al. (2016) brings the mean observed number for this time interval down to 8.8x10^6 cm^{-3}. This recalibration was needed to account for the window absorption of calibrated 185 nm radiation that was neglected in the initial DC3 calibration. This median revised observed OH concentration is consistent with the mean modeled OH concentration of 9.6x10^6 cm^{-3}. These results agree well within uncertainties and support the observed OH.

Another good test of the photochemistry is a comparison between the observed O$_3$ change and the accumulated calculated O$_3$ production rate (Fig. 9). The O$_3$ change is actually slightly larger than the observed O$_3$ because some of the new O$_3$ is partitioned into NO$_2$, so that the quantity of interest is the change in O$_3$ plus the change in NO$_2$. The ozone production rate, $P(O_3)$, can be calculated with the equation

$$P(O_3) = k_{NO+HO2}[NO][HO_2] + \sum_i k_{NO+RO2i}[NO][RO_{2i}] - L(O_3) \qquad (3)$$

where k is a reaction rate coefficient and $L(O_3)$ is the loss terms for ozone. In this case, the loss term was only a few tenths ppbv hr^{-1} (Fig. S10) and can be neglected. These rates are calculated in ppbv min^{-1} and then accumulated at times from 5:45 to 11:15, in order to match the time period over which the DC-8 was sampling the MCS plume. This accumulated ozone production was calculated for the observed HO$_2$ plus modeled RO$_2$ and for the modeled HO$_2$ plus modeled RO$_2$. Modeled RO$_2$ is primarily CH$_3$O$_2$ and CH$_3$CH$_2$O$_2$ and its mixing ratio is half the HO$_2$ mixing ratio above 5 km. HO$_2$ accounts for a little more than half the total O$_3$ production. In order to compare the observed O$_3$ change to that accumulated from calculated O$_3$ production, an ozone offset of 53.4 ppbv was added to the accumulated O$_3$ production at 6:00 local solar time, which is when the ozone production commenced.

Ozone varied by 5-7 ppbv over the legs and was higher on one end of the leg than the other. These variations are smoothed using a 180-minute filter. During the 5 hours from 6:00 to 11:00, the observed O$_3$ change was 14 ppbv, although 2 ppbv of that change was in the final few minutes of observation. For the same time period, the ozone production calculated from modeled HO$_2$ and modeled RO$_2$ was 13 ppbv, and the ozone production calculated from observed HO$_2$ and modeled RO$_2$ was

13 ppbv. These three methods for determining O_3 production agree to well within their uncertainties and provide additional confirmation on the observed and modeled HO_2 and the modeled RO_2.

4 Discussion

These comparisons between median observed and modeled OH, HO_2, and OH reactivity display an agreement that is generally within the combined uncertainties of the observations and model. This agreement within uncertainties generally holds in scatter plots and associated statistics and as a function of altitude, $JO(^1D)$, NO, CO, and the modeled OH reactivity. It also holds for the wide range of environments encountered during DC3 – different altitudes, cloudiness, and sunlight over roughly one third of the continental United States.

A closer look at the figures shows seemingly random differences between observed and modeled OH and HO_2. While most observed and modeled OH, HO_2, and OH reactivity one-minute data are within the combined uncertainties (1σ confidence) of each other (57%), there are sometimes persistent unexplained differences (Fig. S1). An example is from the 21 June flight over Missouri and Illinois (Fig. 8). For both OH and HO_2, there are times when the modeled OH and HO_2 are higher than the measurements, lower than the measurements, and equal to the measurements. At the same time, the measured OH reactivity is sometimes greater than the modeled OH reactivity and sometimes equal to it. These types of discrepancies are proving to be hard to resolve. A simple correlation analysis found no strong correlation between the observed-to-modeled ratio or difference and any model output variable. Employing more sophisticated methods in future work may be more productive.

4.1 Comparing DC3 to Previous Studies

All previous aircraft studies that included measurements of OH and HO_2 have compared these observations to calculations from constrained photochemical box models. There is uncertainty in comparing the results from one study to another because often the instruments, their calibrations, and models are different or have evolved over time. Comparing results from very different environments amplifies this problem. As a result, the comparisons here are restricted to previous studies in air that was heavily influenced by convection.

NO, CO, O_3, and $JO(^1D)$ from DC3 are remarkably similar to those observed in INTEX-A in 2004 during flights over the central and eastern US (Ren et al., 2008) and to those observed from only 7 km to 10 km during HOOVER 2 in summer 2007 during flights over central Europe (Regelin et al., 2013). As in DC3, observed and modeled OH agree to within uncertainties for INTEX-A and HOOVER 2 over their altitude ranges. On the other hand, observed and modeled HO_2 agree to within uncertainties for DC3, HOOVER 2, and INTEX-A up to 8 km, but then observed HO_2 grows to exceed modeled HO_2 by a factor of 3 at 11 km for INTEX-A, in contrast with both DC3 and HOOVER 2 where observed and modeled HO_2 agree to within the combined uncertainties.

One explanation could be the treatment of HO_2NO_2 formation rate in the model. MCMv3.3.1 uses a reaction rate coefficient that takes the much lower low-temperature reaction rate coefficient of the laboratory study of Bacak et al. (2011) into account, while the JPL evaluation (Burkholder et al., 2015) does not. For DC3, using the MCMv3.3.1 rate coefficient, observed-to-modeled OH and HO_2 are 0.85-0.9 at altitudes above 10 km altitude, and modeled HO_2NO_2 is 1.9 times measured, but if the JPL recommended rate is used, then modeled OH and HO_2 both increase by a factor of 1.5 at altitudes above 10 km, shifting the observed-to-modeled ratios to 1.3-1.4, while increasing modeled HO_2NO_2 to 5-10 times that observed (Fig. S10). The JPL recommended reaction rate coefficient was used in the model for INTEX-A, which could explain some of the difference with DC3, except that observed-to-modeled OH ratio should also be a factor of 3 for INTEX-A.

For DC3, observed and modelled HO_2 appear to agree as a function of NO up to about 3 ppbv, which are the highest NO values encountered. For several previous ground-based studies, the observed HO_2 was not obviously greater than the modelled HO_2 until NO reached ~2 ppbv or greater (Martinez et al., 2003; Ren et al., 2003; Shirley et al., 2006; Kanaya et al., 2007; Brune et al., 2016). For aircraft studies, in some cases the observed HO_2 did not obviously exceed the modelled HO_2 until NO approached 2 ppbv (Baier et al, 2017), while in other studies, the obvious exceedance occurred when NO was only a few hundred pptv (Faloona et al., 1999; Ren et al., 2008). Olson et al. (2006) showed that the Faloona et al. (1999) results for the SUCCESS campaign could be explained by the averaging of sharp plumes containing high NO and depleted HO_2 with the surrounding air. They showed that the SONEX results could be mostly explained by including all HO_x precursor observations and updated kinetic rate coefficients and photolysis frequencies in the model. For INTEX-A (Ren et al., 2008), the enhanced NO is in the upper troposphere, where the observed-to-modeled HO_2 reached a factor of 3. It is possible that the HO_2 calibration was in error at low pressure (i.e., higher altitudes), although observed and modelled HO_2 agree in the stratosphere. It is also possible that there were missing HO_2 sources or outdated reaction rates in the model chemistry. We intend to re-examine INTEX-A and other previous NASA DC-8 missions that included ATHOS to see if an updated model can better simulate these HO_2 observations.

The production rates of HO_x (Fig. S11) and O_3 (Fig. S9) are comparable to those found in previous studies (Ren et al., 2008; Olson et al., 2012). Modeled HO_x production is dominated by O_3 photolysis below 8 km, as has been previously observed (Regelin et al., 2013), but HCHO photolysis dominates above 10 km. HO_x production by HONO photolysis essentially balances HO_x loss by HONO formation. The calculated O_3 production rates are also comparable to these other studies, which find production rates of a few ppbv hr^{-1} in the PBL and above 10 km with a small loss at mid-altitude (Fig. S12). A spike in excess of 5 ppbv hr^{-1} was found in a fire plume on 22 June (day-of-year 174), where abundances of both VOCs and NO_x were enhanced.

4.2 Effects of Heterogeneous Chemistry on OH and HO$_2$

These DC3 results indicate that a total uptake coefficient is much less than 1 for aerosol. They also suggest that a total uptake coefficient of 0.2 is probably also too high because the model calculates HO$_2$ values that are much lower than observed HO$_2$ when the aerosol surface area per cm^{-3} of air was greater than 10^{-6} cm^2 cm^{-3}. In the DC3 environment, HO$_x$ has substantial gas-phase loss pathways, making it difficult for heterogeneous chemistry to be dominant when the model uses an uptake coefficient consistent with laboratory studies, except at the largest aerosol surface area per cm^{-3} of air. For the case with a total uptake coefficient of 0.2, HO$_x$ loss including heterogeneous loss is 1.4 times the gas-phase only loss when the aerosol surface area per cm^{-3} of air is 5×10^{-7} cm^{2}cm^{-3}, but grows to 1.5 at 1×10^{-6} cm^{2}cm^{-3} and 2.5 for the few one-minute data points when it is greater than 3×10^{-6} cm^{2}cm^{-3}. This increase in HO$_x$ loss translates into decrease in the modeled HO$_x$, with the decrease changing roughly as the square root of the increase in the HO$_x$ loss.

In DC3, the DC-8 spent hours flying in anvils of the cumulus clouds, which consisted of ice particles. DC3 provides evidence that the HO$_2$ uptake on ice is small. These results are consistent with HO$_2$ results over the western Pacific Ocean (Olson et al., 2004) but not with those over the northern Atlantic (Jeaglé et al., 2000). In Mauldin et al. (1998), a large difference between the observed and modeled OH was found in clouds, but this difference may have been due to the lack of photolysis frequency measurements, which are crucial to test photochemistry in a cloudy environment. In DC3, the DC-8 spent essentially no time in liquid clouds, for which there is evidence of measurable HO$_2$ uptake (Olson et al., 2006; Commane et al., 2010; Whalley et al., 2015). Thus these DC3 results provide constraints of HO$_2$ uptake on aerosol and ice particles, but not on liquid water particles.

In other cleaner environments or dirtier environments with much high aerosol surface area per cm^{-3} of air, heterogeneous chemistry can be a substantial fraction of the entire HO$_x$ loss and thus affect HO$_2$ and OH abundances. Measuring OH and HO$_2$ in these environments will provide a better test of the understanding of HO$_2$ heterogeneous chemistry than DC3 did.

5 Conclusions

The general agreement between the observed and modeled OH and HO$_2$ for the complex DC3 environment is encouraging. It suggests that a photochemical box model can simulate the observed OH and HO$_2$ to well within combined uncertainties, if properly constrained with measurements of other chemical species, photolysis frequencies, and environmental conditions. On the other hand, it is difficult to explain the unexpected deviations between observed and modeled OH and HO$_2$, such as is observed in Fig. 8 or Fig. S1. Neither heterogeneous chemistry nor organic peroxyl chemistry are able to explain these deviations.

There are other possible causes for these discrepancies. First, it can be difficult to maintain instrument calibrations for not only OH and HO_2 but also for all the other measurements that were used to constrain the model to calculate OH and HO_2. Second, the simultaneous measurements need to be properly conditioned so that they can be used as model constraints. This process includes filling in isolated missing values because, if this was not done, the constraining data set would be sparse. For DC3,

5   using the merged data set with no interpolation is less than 10% of the full data set, but the observed and modeled OH and HO_2 have essentially the same relationships as with the interpolated data set (Table S21). Third, the model parameters, such as integration times and decay times, must be set up so that the model calculations represent the observations and their variations. Varying these times caused a range of modeled values that was far smaller than the large observed-to-modeled differences, as seen in Fig. S1. For DC3, the one-minute data are adequate for the timescale of variations for most cases, except

10   in small fire plumes and some spikes in lightning NO_x in the anvil. Fourth, multiple methods are needed to determine if differences between observations and model are significant. For DC3, the comparisons between observations and models are robust despite the method of comparison. Thus, none of these appear to be the cause of the unexplained deviations between observed and modeled OH and HO_2. A more thorough model uncertainty and sensitivity analysis could unveil the cause.

15   Even with these observed-to-modeled discrepancies, the general agreement for observed and modeled OH and HO_2 suggests that current photochemical models can simulate observed atmospheric oxidation processes even around clouds to within these combined uncertainties. Reducing these uncertainties will enable comparisons of observed and modeled OH and HO_2 to provide a more stringent test of the understanding of atmospheric oxidation chemistry and thus to lead to an improvement in that understanding.

20   **Code Availability**

The Matlab code used for the zero-dimensional photochemical box modelling with the MCMv3.3.1 mechanism can be downloaded from the website https://sites.google.com/site/wolfegm/models. The manuscript describing this model is Wolfe, G.M, M.R. Marvin, S.J. Roberts, K.R. Travis, and J. Liao, The Framework for 0-D Atmospheric Modeling (F0AM) v3.1, *Geoscientific Model Development*, 9, 3309-3319, doi: 10.5194/gmd-9-3309-2016, 2016.

25   **Data Availability**

The merge file for the DC3 DC-8 data and the updated OH, HO_2, and OH reactivity numbers can be accessed from http://data. eol.ucar.edu/ or http://www-air.larc.nasa.gov/cgi-bin/ArcView/dc3-seac4rs, doi:10.5067/Aircraft/DC3/DC8/Aerosol-TraceGas

Author Contribution

All authors contributed DC3 measurements that are critical for the modeling and comparison of modeled and measured OH and HO$_2$ in this manuscript. W. Brune wrote the manuscript and made edits provided by the co-authors before submitting the manuscript.

5 Competing Interests

The authors declare that they have no conflicts of interest.

Acknowledgments

The Deep Convective Clouds and Chemistry (DC3) experiment is sponsored by the U.S. National Science Foundation (NSF), the National Aeronautics and Space Administration (NASA), the National Oceanic and Atmospheric Administration (NOAA), and the Deutsches Zentrum fuer Luftund Raumfahrt (DLR). Archived field data can be accessed from http://data. eol.ucar.edu/ or http://www-air.larc. nasa.gov/cgi-bin/ArcView/dc3-seac4rs. Data provided by NCAR/EOL are supported by the National Science Foundation. Acetone/propanal measurements aboard the DC-8 during DC3 were supported by the Austrian Federal Ministry for Transport, Innovation, and Technology (BMVIT) through the Austrian Space Applications Programme (ASAP) of the Austrian Research Promotion Agency (FFG). Support for ATHOS and OHR measurements aboard the NASA DC-8 during DC3 comes from NASA grant NNX12AB84G. We thank NASA management, pilots, and operations personnel for the opportunity to gather these observations, the people of Salina, KS for hosting us and providing excellent facilities, G. Wolfe for his publically available F0AM model framework, and the University of Leeds for the publically available MCMv3.3.1 photochemical model. We also thank J. Thornton for his insights into HO$_2$ heterogeneous chemistry, and P. Lawson, P. Wennberg, J. Crounse, and J. St. Clair for the use of their measurements.

20 References

Apel, E. C.; Olson, J. R.; Crawford, J. H., Hornbrook, R.S., Hills, A.J., Cantrell, C.A., Emmons, L.K., Knapp, D.J., Hall, S., Mauldin, R.L., Weinheimer, A.J., Fried, A., Blake, D.R., Crounse, J.D., St Clair, J.M., Wennberg, P.O., Diskin, G.S., Fuelberg, H.E., Wisthaler, A., Mikoviny, T., Brune, W., Riemer, D.D., Impact of the deep convection of isoprene and other reactive trace species on radicals and ozone in the upper troposphere, Atmospheric Chemistry and Physics, 12, 1135-1150, DOI: 10.5194/acp-12-1135-2012, 2012.

Apel, E.C., Hornbrook, R.S., Hills, A.J., Blake, N.J., Barth, M.C., Weinheimer, A., Cantrell, C., Rutledge, S.A., Basarab, B., Crawford, J., Diskin, G., Homeyer, C.R., Campos, T., Flocke, F., Fried, A., Blake, D.R., Brune, W., Pollack, I., Peischl, J. Ryerson, T., Wennberg, P.O., Crounse, J.D., Wisthaler, A., Mikoviny, T., Huey, G., Heikes, B., O'Sullivan, D., and Riemer, D.D., Upper tropospheric ozone production from lightning NOx-impacted convection: Smoke ingestion case study from the DC3 campaign. Journal of Geophysical Research-Atmospheres, 120 (6):2505-2523, 2015.Assaf, E., Sheps, L., Whalley, L.,

Heard, D., Tomas, A., Schoemaecker, C., Fittschen, C., The Reaction between CH3O2 and OH Radicals: Product Yields and Atmospheric Implications, Environ. Sci. Technol., 51, 2170−2177, 2017, DOI: 10.1021/acs.est.6b06265.

Bacak, A., Cooke, M. C., Bardwell, M. W., McGillen, M. R., Archibald, A. T., Huey, L. G., Tanner, D., Utembe, S. R., Jenkin, M. E., Derwent, R. G., et al., Kinetics of the $HO_2 + NO_2$ Reaction: On the Impact of New Gas-Phase Kinetic Data for the Formation of HO_2NO_2 on HO_x, NO_x and HO_2NO_2 Levels in the Troposphere, Atmos. Environ., 45, 6414-6422, 2014.

Baier, B.C., W.H. Brune, D.O. Miller, D. Blacke, R. Long, A. Wisthaler, C. Cantrell, A. Fried, B. Heikes, S. Brown, E. McDuffie, F. Flocke, E. Apel, L. Kaser, and A. Weinheimer(2017), Higher measured than modeled ozone production at increased NOx levels in the Colorado Front Range, Atmospheric Chemistry and Physics, 17(18), 11273-11292, doi:10.5194/acp-17-11273-2017, 2017.

Barth, M.C., Cantrell, C.A., Brune, W.H., Rutledge, S.A, Crawford, J.H., Huntrieser, H., Carey, L.D., MacGorman, D., Weisman, M., Pickering, K.E., Bruning, E., Anderson, B., Apel, E., Biggerstaff, M., Campos, T., Campuzano-Jost, P. Cohen, R., Crounse, J., Day, D.A., Diskin, G., Flocke, F., Fried, A., Garland, C., Heikes, B., Honomichl, S., Hornbrook, R., Huey, L.G., Jimenez, J.L., Lang, T., Lichtenstern, M., Mikoviny, T., Nault, B., O'Sullivan, D., Pan, L.L., Peischl, J., Pollack, I., Richter, D., Riemer, D., Ryerson, T., Schlager, H., St Clair, J., Walega, J., Weibring, P., Weinheimer, A., Wennberg, P., Wisthaler, A., Wooldridge, P.J., and Ziegler, C., The Deep Convective Clouds and Chemsitry (DC3) Field Campaign, Bulletin of the American Meteorological Society, 96, 1281-1309, 2015.

Barth, M.C., Bela, M.M., Fried, A., Wennberg, P.O., Crounse, J.D., St Clair, J.M., Blake, N.J., Blake, D.R., Homeyer, C.R., Brune, W.H., Zhang, L., Mao, J., Ren, X., Ryerson, T.B., Pollack, I.B., Peischl, J., Cohen, R.C., Nault, B.A., Huey, L.G., Liu, X., and Cantrell, C.A., Convective transport and scavenging of peroxides by thunderstorms observed over the central US during DC3, J. Geophys. Res. Atmos., 121, 4272-4295, 2016.

Bernt, T., W. Scholz, B. Mentler, L. Fischer, H. Herrmann, M. Kumala, and A. Hansel, Accretion Product Formation from Self- and Cross-Reactions of RO_2 Radicals in the Atmosphere, Angew. Chem. Int. Ed., 57, 3820 −3824, 2018, DOI: 10.1002/anie.201710989.Bozem, H., Fischer, H., Gurk, C., Schiller, C. L., Parchatka, U., Koenigstedt, R., Stickler, A., Martinez, M., Harder, H., Kubistin, D., Williams, J., Eerdekens, G., and Lelieveld, J., Influence of corona discharge on the ozone budget in the tropical free troposphere: a case study of deep convection during GABRIEL, Atmos. Chem. Phys., 14, 8917-8931, doi.org/10.5194/acp-14-8917-2014, 2014.

Brune, WH, BC Baier, J Thomas, X Ren, RC Cohen, SE Pusede, EC Browne, AH Goldstein, DR Gentner, FN Keutsch, JA Thornton, S Harrold, FD Lopez-Hilfiker, and PO Wennberg, Ozone production chemistry in the presence of urban plumes. Faraday Discussions, 189:169-189, 2016.

Burkholder, J.B., Sander, S.P., Abbatt, J., Barker, J.R., Huie, R.E., Kolb, C.E., Kurylo, M.J., Orkin, V.L., Wilmouth, D.M., and Wine, P.H., "Chemical Kinetics and Photochemical Data for Use in Atmospheric Studies, Evaluation No. 18," JPL Publication 15-10, Jet Propulsion Laboratory, Pasadena, 2015, http://jpldataeval.jpl.nasa.gov, 2015.

Cazorla M, Wolfe GM, Bailey SA, Swanson AK, Arkinson HL, Hanisco TF. A new airborne laser-induced fluorescence instrument for in situ detection of formaldehyde throughout the troposphere and lower stratosphere. Atmos Meas Tech. 2015;8:541–552. doi: 10.5194/amt-8-541-2015.

Chen, S., Brune, W.H., Oluwole, O.O., Kolb, C.E., Bacon, F., Li, G.Y., Rabitz, H., Global Sensitivity Analysis of the Regional Atmospheric Chemical Mechanism: An Application of Random Sampling-High Dimensional Model Representation to Urban Oxidation Chemistry, Environmental Science and Technology, 46, 11162-11170   DOI: 10.1021/es301565w, 2012.

Chatfield, R. B., and Crutzen, P.J., Sulfur dioxide in remote oceanic air: Cloud transport of reactive precursors, J. Geophys. Res., 89, 7111–7132, doi:10.1029/JD089iD05p07111, 1984.

Christian, K. E., Brune, W.H., and Mao, J.Q., Global sensitivity analysis of the GEOS-Chem chemical transport model: ozone and hydrogen oxides during ARCTAS (2008). Atmospheric Chemistry and Physics, 17, 3769-3784, 2017.

Colman, J.J., A.J. Swanson, S. Meinardi, B.C. Sive, D.R. Blake, and F.S. Rowland, Description of the Analysis of a Wide Range of Volatile Organic Compounds in Whole Air Samples Collected during PEM-Tropics A and B, Anal. Chem., 73, 3723-3731, 2001.

Commane, R., Floquet, C. F. A., Ingham, T., Stone, D., Evans, M. J., and Heard, D. E.: Observations of OH and HO_2 radicals over West Africa, Atmos. Chem. Phys., 10, 8783-8801, https://doi.org/10.5194/acp-10-8783-2010, 2010.

Crawford, J; Olson, J., Davis, D., Chen, G., Barrick, J., Shetter, R., Lefer, B., Jordan, C., Anderson, B., Clarke, A., Sachse, G., Blake, D., Singh, H., Sandolm, S., Tan, D., Kondo, Y., Avery, M. Flocke, F., Eisele, F., Mauldin, L. Zondlo, M., Brune, W., Harder, H., Martinez, M., Talbot, R., Bandy, A., Thornton, D., Clouds and trace gas distributions during TRACE-P, J. Geophys. Res. Atmos., 108 (D21), art. no.-8818, 2003.Crounse, J. D., K. A. McKinney, A. J. Kwan, and P. O. Wennberg, Measurement of gas-phase hydroperoxides by chemical ionization mass spectrometry, Anal. Chem., 78(19), 6726-6732, 2006

Day, D.A., P. J. Wooldridge, M. B. Dillon, J. A. Thornton, and R. C. Cohen, A thermal dissociation laser-induced fluorescence instrument for in situ detection of NO_2, peroxy nitrates, alkyl nitrates, and HNO_3, J. Geophys. Res. 107, 4046, 2002.

DC3 Data, doi: 10.5067/Aircraft/DC3/DC8/Aerosol-TraceGas, 2017.

Faloona, I.C., Tan, D., Lesher, R.L., Hazen, N.L, Frame, C.L., Simpas, J.B., Harder, H., Martinez, M., Di Carlo, P., Ren, X.R., Brune, W.H., A laser-induced fluorescence instrument for detecting tropospheric OH and HO_2: Characteristics and calibration, J. Atmos. Chem., 47, 139-167, 2004.

Feiner, P.A., Brune, W.H., Miller, D.O., Zhang, L., Cohen, R.C., Romer, P.S., Goldstein, A.H., Keutsch, F.N., Skog, K.M., Wennberg, P.O., Nguyen, T.B., Teng, A.P., DeGouw, J., Koss, A., Wild, R.J., Brown, S.S., Guenther, A., Edgerton, E., Baumann, K., and Fry, J.L., Testing Atmospheric Oxidation in an Alabama Forest. Journal of the Atmospheric Sciences, 73 (12):4699-4710, 2016.

Fuchs, H., Bohn, B., Hofzumahaus, A., Holland, F., Lu, K. D., Nehr, S., Rohrer, F., and Wahner, A. (2011), Detection of HO_2 by laser-induced fluorescence: Calibration and interferences from RO_2 radicals, Atmos. Meas. Tech., 4, 1209–1225Fuchs, H., Novelli, A., Rolletter, M., Hofzumahaus, A., Pfannerstill, E. Y., Kessel, S., Edtbauer, A., Williams, J., Michoud, V.,

Dusanter, S., Locoge, N., Zannoni, N., Gros, V., Truong, F., Sarda-Esteve, R., Cryer, D. R., Brumby, C. A., Whalley, L. K., Stone, D., Seakins, P. W., Heard, D. E., Schoemaecker, C., Blocquet, M., Coudert, S., Batut, S., Fittschen, C., Thames, A. B., Brune, W. H., Ernest, C., Harder, H., Muller, J. B. A., Elste, T., Kubistin, D., Andres, S., Bohn, B., Hohaus, T., Holland, F., Li, X., Rohrer, F., Kiendler-Scharr, A., Tillmann, R., Wegener, R., Yu, Z., Zou, Q., and Wahner, A., Comparison of OH reactivity measurements in the atmospheric simulation chamber SAPHIR, Atmos. Meas. Tech., 10, 4023-4053, https://doi.org/10.5194/amt-10-4023-2017, 2017.

Hard, T. M., O'Brian, R. J., Chan, C. Y., and Mehrabzadeh, A. A., Tropospheric free radical determination by FAGE, *Environ. Sci. Technol.*, 18, 768–777, 1984.

Huey, L. G., Measurement of trace atmospheric species by chemical ionization mass spectrometry: Speciation of reactive nitrogen and future directions, Mass Spectrom. Rev., 26(2), 166-184, 2007.

Jacob, D.J., Heterogeneous chemistry and tropospheric ozone, Atm. Environ., 34, 2131-2159, 2007.

Jaeglé, L., et al., Observed OH and HO_2 in the upper troposphere suggest a major source from convective injection of peroxides, *Geophys. Res. Lett.*, 24, 3181–3184, doi:10.1029/97GL03004, 1997.

Jaeglé, L., Jacob, D., Brune, W., Faloona, I., Tan, D., Heikes, B., Kondo, Y., Sachse, G., Anderson, B., Gregory, G., Singh, H., Pueschel, R., Ferry, G., Blake, D., Shetter, R., Photochemistry of HO_x in the upper troposphere at northern latitudes. J. Geophys. Res., 105, 3877-3892, 2000.

Jenkin, M. E., Saunders, S. M., Wagner, V., and Pilling, M. J., Protocol for the development of the Master Chemical Mechanism, MCM v3 (Part B): tropospheric degradation of aromatic volatile organic compounds, Atmos. Chem. Phys., 3, 181-193, https://doi.org/10.5194/acp-3-181-2003, 2003.

Kanaya, Y., R. Cao, H. Akimoto, M. Fukuda, Y. Komazaki, Y. Yokouchi, M. Koike, H. Tanimoto, N. Takegawa and Y. Kondo, Urban photochemistry in central Tokyo: 1. Observed and modeled OH and HO2 radical concentrations during the winter and summer of 2004, J. Geophys. Res., 112, D21312, DOI: 10.1029/2007jd008670, 2007.

Kovacs, T., and Brune, W., Total OH Loss Rate Measurement. J. Atmos. Chem., 39, 105-122, 2001.

Kubistin, D., Harder, H., Martinez, M., Rudolf, M., Sander, R., Bozem, H., Eerdekens, G., Fischer, H., Gurk, C., Kluepfel, T., Koenigstedt, R., Parchatka, U., Schiller, C.L., Stickler, A., Taraborrelli, D., Williams, J., and Lelieveld, J., Hydroxyl radicals in the tropical troposphere over the Suriname rainforest: comparison of measurements with the box model MECCA, Atmos. Chem. Phys., 10, 9705-9778, doi:10.5194/acp-10-9705-2010, 2010.

Lakey, P.S.J, George, I.J., Baeza-Romero, M.T., Whalley, L.K., and Heard, D.E., Organics Substantially Reduce HO_2 Uptake onto Aerosols Containing Transition Metal ions, J. Phys. Chem. A, 120, 1421−1430, DOI: 10.1021/acs.jpca.5b06316, 2015.

Lakey P.S.J., Berkemeier, T., Krapf, M., Dommen, J., Steimer, S.S., Whalley, L.K., Ingham, T., Baeza-Romero, M.T., Pöschl, U., Shiraiwa, M., Ammann, M., Heard, D.E., The effect of viscosity and diffusion on the HO_2 uptake by sucrose and secondary organic aerosol particles, Atmospheric Chemistry and Physics, 16, 13035-13047, 2016.

Logan, J. A., Prather, M. J., Wofsy, S. C., and McElroy, M. B., Tropospheric chemistry: A global perspective, *J. Geophys. Res.,* 86, 7210–7254, 1981.

Mao J., Ren, X., Brune, W.H., Olson, J.R., Crawford, J.H., Fried, A., Huey, L.G., Cohen, R.C., Heikes, B., Singh, H.B., Blake, D.R., Sachse, G.W., Diskin, G.S., Hall, S.R., and Shetter, R.E., Airborne measurement of OH reactivity during INTEX-B, *Atmospheric Chemistry and Physics*, **9**, 163-173, 2009.

Mao, J., Ren, X., Zhang, L., Van Duin, D.M., Cohen, R.C., Park, J.-H., Goldstein, A.H., Paulot, F., Beaver, M.R., Crounse, J.D., Wennberg, P.O., DiGangi, J.P., Henry, S.B., Keutsch, F.N., Park, C., Schade, G.W., Wolfe, G.M., Thornton, J.A., and Brune, W.H., Insights into hydroxyl measurements and atmospheric oxidation in a California forest, Atmos. Chem. Phys., **12**, 8009–8020, 2012.

Mao J., Jacob, D.J., Evans, M.J., Olson, J.R., Ren, X., Brune, W.H., St. Clair, J.M., Crounse, J.D., Spencer, K.M., Beaver, M.R., Wennberg, P.O., Cubison, M.J., Jimenez, J.L., Fried, A., Weibring, P., Walega, J.G., Hall, S.R., Weinheimer, A.J., Cohen, R.C., Chen, G., Crawford, J.H., McNaughton, C., Clarke, A.D., Jaegl´e, L., Fisher, J.A., Yantosca, R.M., Le Sager, P., and Carouge, C., Chemistry of hydrogen oxide radicals (HOx) in the Arctic troposphere in spring, Atmospheric Chemistry and Physics, 10, 5823-5838, 2010.

Martinez, M, H. Harder, T.A. Kovacs, J.B. Simpas, J. Bassis, R. Lesher, W.H. Brune, G.J. Frost, E.J. Williams, C.A. Stroud, B.T. Jobson, J.M. Roberts, S.R. Hall, R.E. Shetter, B. Wert, A. Fried, B. Alicke, J. Stutz, V.L. Young, A.B. White, R.J. Zamora, OH and HO2 concentrations, sources, and loss rates during the Southern Oxidants Study in Nashville, Tennessee, summer 1999, J. Geophys. Res., 108 (D19), art. no.-4617, 2003.

Mauldin III, R. L., Tanner, D. J., Frost, G. J., Chen, G., Prevot, A. S. H., Davis, D. D., and Eisele, F. L., OH measurements during ACE-1: observations and model comparisons, J. Geophys. Res. Atmos., 103, 16713–16729, 1998.

Mielke, L.H., D. E. Erickson, S. A. McLuckey, M. Müller, A. Wisthaler, A. Hansel, P. B. Shepson, Development of a Proton-Transfer Reaction-Linear Ion Trap Mass Spectrometer for Quantitative Determination of Volatile Organic Compounds, Anal. Chem 80(21), 8171-8177, DOI:10.1021/ac801328d, 2008

Nault, B.A., Garland, C., Wooldridge, P.J., Brune, W.H., Campuzano-Jost, J., Crounse, J.D., Day, D.A., Dibb, J., Hall, S.R., Huey, L.G., Jimenez, J.L., Liu, X.X., Mao, J.Q., Mikoviny, T., Peischl, J., Pollack, I.B., Ren, X.R., Ryerson, T.B., Scheuer, E., Ullmann, K., Wennberg, P.O., Wisthaler, A., Zhang, L., and Cohen, R.C., Observational Constraints on the Oxidation of NOx in the Upper Troposphere, Journal of Physical Chemistry a, 120 (9):1468-1478, 2016.

Nault, B. A., Laughner, J. L., Wooldridge, P. J., Crounse, J. D., Dibb, J., Diskin, G., … Cohen, R. C., Lightning NOx emissions: reconciling measured and modeled estimates with updated NOx chemistry. Geophysical Research Letters, 44, 9479–9488. https://doi.org/ 10.1002/2017GL074436, 2017.

Olson, J. R., et al., Testing fast photochemical theory during TRACE-P based on measurements of OH, HO2, and CH2O, J. Geophys. Res., 109, D15S10, doi:10.1029/2003JD004278, 2004.

Olson, J. R., Crawford, J.H., Chen, G., Brune, W.H., Faloona, I.C., Tan, D., Harder, H., and Martinez, M., A reevaluation of airborne HOx observations from NASA field campaigns, J. Geophys. Res., Atmos., 111, D10301, doi:10.1029/2005JD006617, 2006.

Olson, J.R., Crawford, J.H., Brune, W., Mao, J., Ren, X., Fried, A., Anderson, B., Apel, E., Beaver, M., Blake, D., Chen, G., Crounse, J., Dibb, J., Diskin, G., Hall, S.R., Huey, L.G., Knapp, D., Richter, D., Riemer, D., St. Clair, J., Ullmann, K., Walega, J., Weibring, P., Weinheimer, A., Wennberg, P., and Wisthaler, A., An analysis of fast photochemistry over high northern latitudes during spring and summer using in-situ observations from ARCTAS and TOPSE, Atmos. Chem. Phys.,

5   12, 6799-6825, https://doi.org/10.5194/acp-12-6799-2012, 2012.Pickering, K. E., Thompson, A.M., Dickerson, R.R., Luke, W.T., McNamara, D.P., Greenberg, J.P., and Zimmerman, P.R., Model calculations of tropospheric ozone production potential following observed convective events, J. Geophys. Res., 95, 14 049–14 062, doi:10.1029/JD095iD09p14049, 1990.

Pollack, I. B., B. M. Lerner, and T. B. Ryerson, Evaluation of ultraviolet light-emitting diodes for detection of atmospheric NO_2 by

10   photolysis-chemiluminescence, J. Atmos. Chem., 65(2), 111–125, doi:10.1007/s10874-011-9184-3, 2001.

Pollack, I. B., et al., Airborne quantification of upper tropospheric NOx production from lightning in deep convective storms over the United States Great Plains, *J. Geophys. Res. Atmos.*, 121, 2002–2028, doi:10.1002/ 2015JD023941, 2016.

Ravetta, F., Jacob, D.J., Brune, W.H., Tan, D., Faloona, I.F., Heikes, B.J., Anderson, B., Blake, D.R., Gregory, G.L., Sachse, G.W., Sandholm, S.T., Shetter, R.E., Singh, H.E., Talbot, R.W., Experimental evidence for the importance of convected

15   methylhydroperoxide as a source of hydrogen oxide (HOx) radicals in the tropical upper troposphere. J. Geophys. Res., 106, 32,709, 2001.

Regelin, E., Harder, H., Martinez, M., Kubistin, D., Tatum Ernest, C., Bozem, H., Klippel, T., Hosaynali-Beygi, Z., Fischer, H., Sander, R., Jöckel, P., Königstedt, R., and Lelieveld, J., HO_x measurements in the summertime upper troposphere over Europe: a comparison of observations to a box model and a 3-D model, Atmos. Chem. Phys., 13, 10703-10720,

20   https://doi.org/10.5194/acp-13-10703-2013, 2013.

Ren, X.R., H. Harder, M. Martinez, R.L. Lesher, A. Oliger, T. Shirley, J. Adams, J.B. Simpas, W.H. Brune, HOx concentrations and OH reactivity observations in New York City during PMTACS-NY2001, Atmos. Environ., 37, (26), 3627-3637, 2003.

Ren, X.R., Olson, J.R., Crawford, J.H, Brune, W.H., Mao, J.Q., Long, R.B., Chen, Z., Chen, G., Avery, M.A., Sachse, G.W.,

25   Barrick, J.D., Diskin, G.S., Huey, L.G., Fried, A., Cohen, R.C., Heikes, B., Wennberg, P.O., Singh, H.B., Blake, D.R., Shetter, R.E., HO_x chemistry during INTEX-A 2004: Observation, model calculation, and comparison with previous studies, J. Geophys. Res. Atmos., 113, D5, doi: D05319, 2008.

Ren, X., Mao, J., Brune, W.H., Cantrell, C.A., Mauldin, R.L., Hornbrook, R.S., Kosciuch, E., Olson, J.R., Crawford, J.H., Chen, G., Singh, H.B., Airborne intercomparison of HOx measurements using laser-induced fluorescence and chemical

30   ionization mass spectrometry during ARCTAS, Atmospheric Measurement Techniques, 5, 2025-2037, DOI: 10.5194/amt-5-2025-2012, 2012.

Ridley, B. A., Dye, J., Walega, J.G., Zheng, J., Grahek, F.E., and Rison, W., On the production of active nitrogen by thunderstorms over New Mexico, J. Geophys. Res., Atmos., 101, 20,985–21,005, doi:10.1029/96JD01706, 1996.

Ryerson, T. B., E. J. Williams, and F. C. Fehsenfeld, An efficient photolysis system for fast-response NO2 measurements, J. Geophys. Res., 105, 26,447–26,461, 2000.

Sachse, G. W., J. E. Collins, G. F. Hill, L. O. Wade, L. G. Burney, and J. A. Ritter, Airborne tunable diode-laser sensor for high-precision concentration and flux measurements of carbon-monoxide and methane, Proc. SPIE, 1433, 157–166, 1991.

5   Shirley, T.R., W. H. Brune, X. Ren, J. Mao, R. Lesher, B. Cardenas, R. Volkamer, L. T. Molina, M. J. Molina, B. Lamb, E. Velasco, T. Jobson, and M. Alexander, Atmospheric oxidation in the Mexico City Metropolitan Area (MCMA) during April 2003, Atmos. Chem. Phys., 6, 2753-2765, 2006.

Vay, S. A., B. E. Anderson, G. W. Sachse, J. E. Collins, Jr., J. R. Podolske, C. H. Twohy, B. Gandrud, K. R. Chan, S. L. Baughcum, and H. A. Wallio, DC-8-based observations of aircraft CO, CH_4, N_2O, and $H_2O(g)$ emission indices during

10   SUCCESS, Geophys. Res. Lett., 25, (10), 1717-1720, 1998.Saunders, S. M., Jenkin, M. E., Derwent, R. G., and Pilling, M. J., Protocol for the development of the Master Chemical Mechanism, MCM v3 (Part A): tropospheric degradation of non-aromatic volatile organic compounds, Atmos. Chem. Phys., 3, 161-180, https://doi.org/10.5194/acp-3-161-2003, 2003.

Schumann, U., and Huntrieser, H., The global lightning-induced nitrogen oxides source, Atmos. Chem. Phys., 7(14), 3823–3907, 2007.

15   Stone, D., Evans, M.J., Commane, R., Ingham, T., Floquet, C.F.A., McQuaid, J.B., Brookes, D.M., Monks, P.S., Purvis, R., Hamilton, J.F., Hopkins, J., Lee, J., Lewis, A.C., Stewart, D., Murphy, J.G., Mills, G., Oram, D., Reeves, C.E., and Heard, D.E., HO_x observations over West Africa during AMMA: impact of isoprene and NO_x, Atmos. Chem. Phys., 10, 9415-9429, doi:10.5194/acp-10-9415-2010, 2010.

Stone, D., Whalley, L.K, and Heard, D.E., Tropospheric OH and HO2 radicals: field measurements and model comparisons,

20   Chem. Soc. Rev., 41, 6348–6404, 2014.

Tang, M.J., R.A. Cox, and M. Kalberer (2014), Compilation and evaluation of gas phas diffusion coefficients of reactive trace gases in the atmosphere: volume 1. Inorganic compounds, *Atmos. Chem. Phys.* 14, 9233-9247, doi:10.5194/acp-14-9233-2014.

Thompson, A.M., and Stewart, R.W., Effect of chemical kinetics uncertainties on calculated constituents in a tropospheric

25   photochemical model, J. Geophys. Res., Atmos., 96, 13089-13108, doi: 10.1029/91JD01056, 1991.

Thornton, J.A., P. J. Wooldridge, and R. C. Cohen, Atmospheric NO2: In Situ Laser-Induced Fluorescence Detection at Parts per Trillion Mixing Ratios, Anal. Chem. 72, 528–539, 2000.

Thornton, J. A., Jaegle´, L., and McNeill, V.F., Assessing known pathways for HO 2 loss in aqueous atmospheric aerosols: Regional and global impacts on tropospheric oxidants, J. Geophys. Res., Atmos., 113, D05303, doi:10.1029/2007JD009236,

30   2008.

Wennberg, P.O., et al., Hydrogen radicals, nitrogen radicals, and the production of O_3 in the upper troposphere, Science, 279, 49-53, 1998.

Whalley, L. K., Stone, D., George, I. J., Mertes, S., van Pinxteren, D., Tilgner, A., Herrmann, H., Evans, M. J., and Heard, D. E. (2015), The influence of clouds on radical concentrations: observations and modelling studies of HO_x during the Hill Cap

Cloud Thuringia (HCCT) campaign in 2010, Atmos. Chem. Phys., 15, 3289-3301, https://doi.org/10.5194/acp-15-3289-2015.

Wolfe, G.M, Marvin, M.R., Roberts, S.J., Travis, K.R., and Liao, J., The Framework for 0-D Atmospheric Modeling (F0AM) v3.1, Geoscientific Model Development, 9, 3309-3319, doi: 10.5194/gmd-9-3309-2016, 2016.

5 York, D., N. Evensen, M. Martinez, J. Delgado, Unified equations for the slope, intercept, and standard errors of the best straight line" Am. J. Phys. 72 (3), 2004.
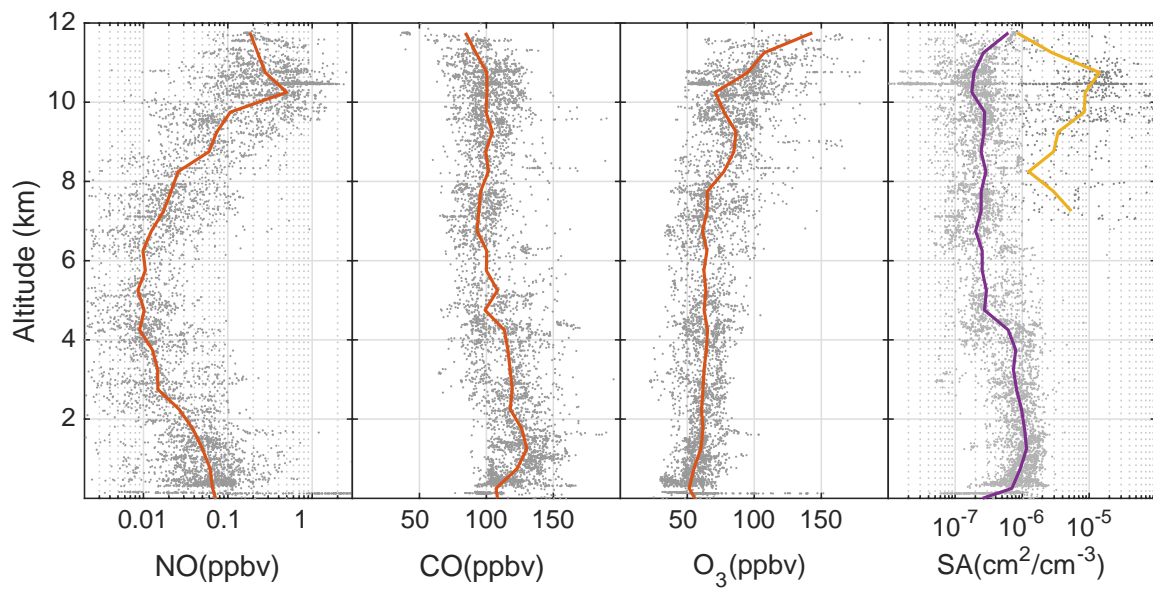
Figure 1. Altitude profiles of median NO, CO, O$_3$, and aerosol (purple) and ice (yellow) surface area (SA). Grey points are individual one-minute data, while median values are represented by the lines. These data are for the entire DC3 study.
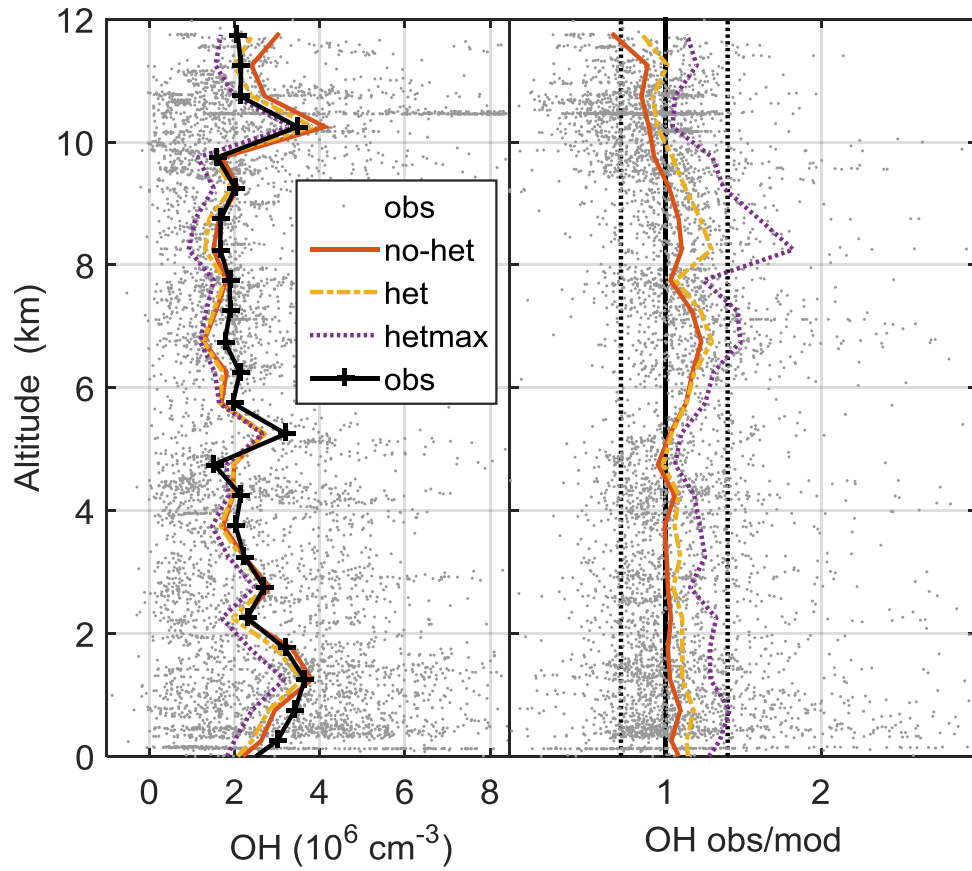
Figure 2. Median measured and modeled OH as a function of altitude (left); median ratio of observed-to-modeled OH as a function of altitude (right) for the three models. Gray points are individual 1-minute OH observations and ratios of observed-to-no-heterogeneous modeled OH. Dotted vertical black lines on right (1/1.4, 1.4) are approximate indicators of measurement-model agreement.
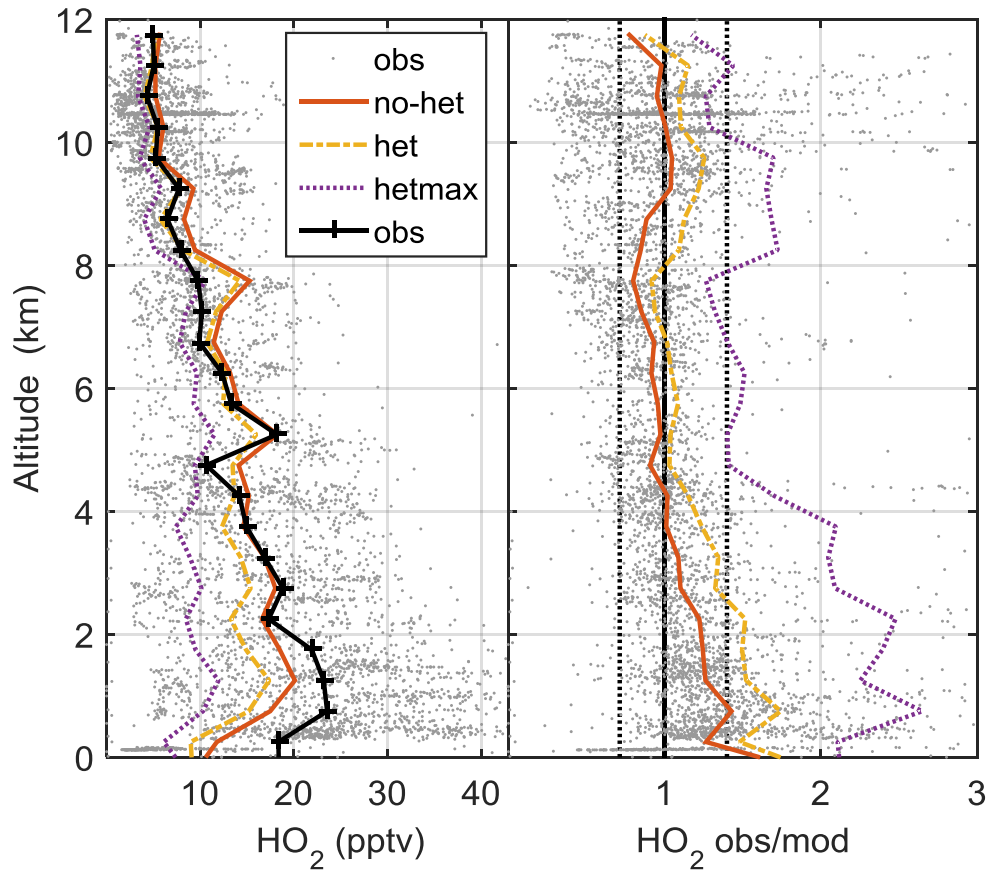
Figure 3. Median measured and modeled HO₂ as a function of altitude (left); median ratio of observed-to-modeled HO₂ as a function of altitude (right) for the three models. Gray points are individual 1-minute OH observations and ratios of observed-to-no-heterogeneous modeled OH. Dotted vertical black lines on right (1/1.4, 1.4) are approximate indicators of measurement-model agreement.
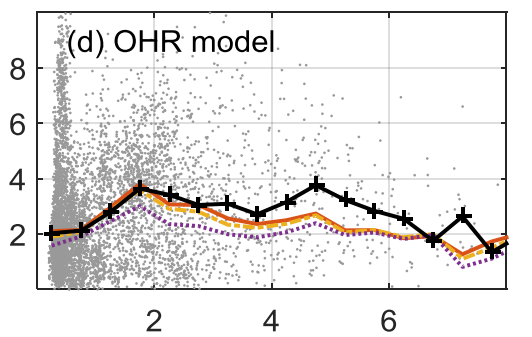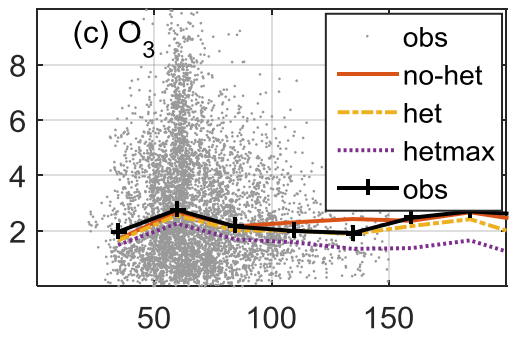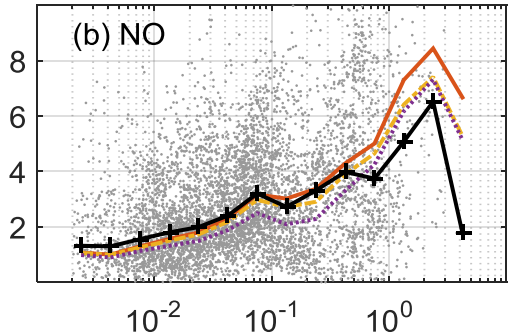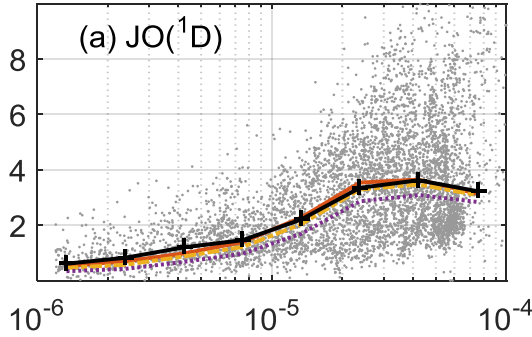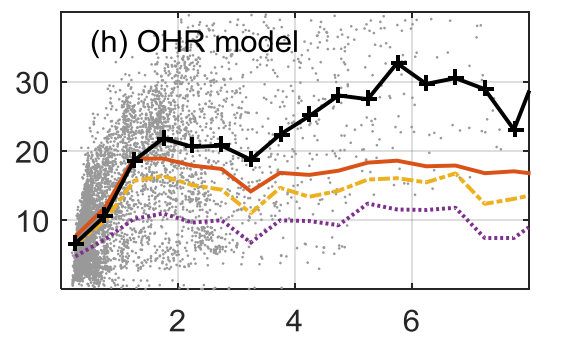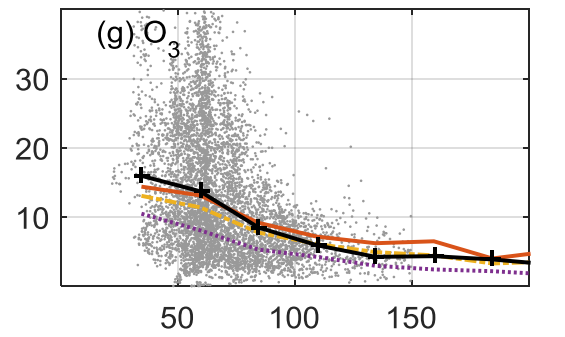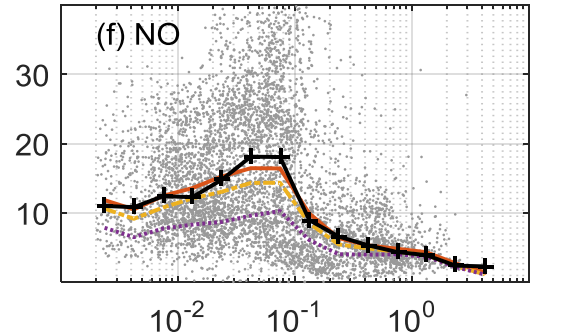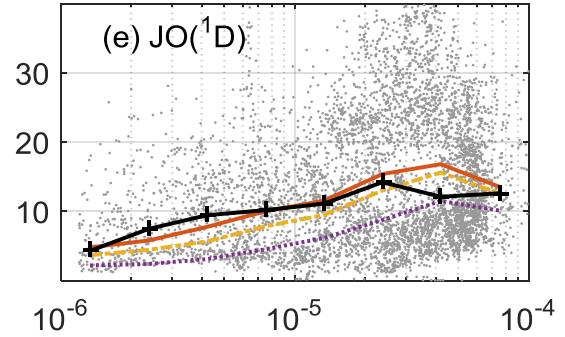
Figure 4. Measured and modeled OH (left) and HO$_2$ (right) as a function of controlling variables: JO(^{1}D) in s^{-1}, NO in ppbv, O$_3$ in ppbv, and modeled OH reactivity in s^{-1}. On the left, OH is in units of 10^6 cm^{-3}; on the right, HO$_2$ is in units of pptv.
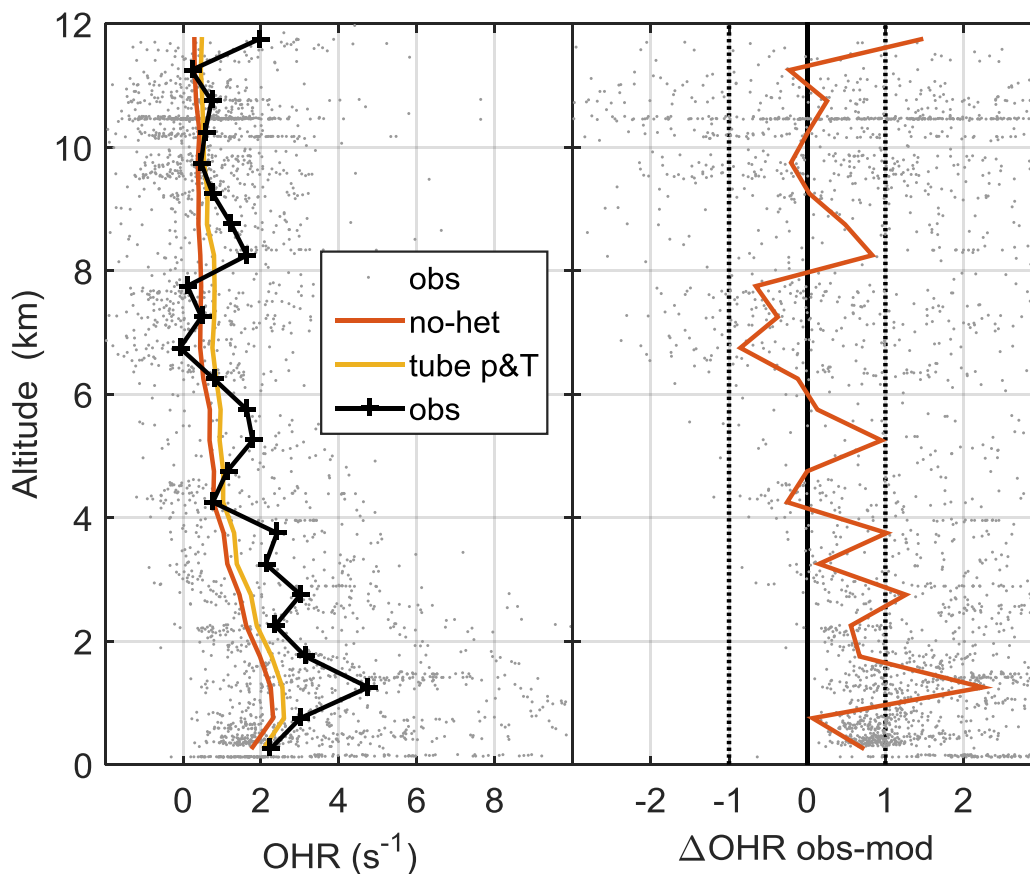
Figure 5. Median observed and model-calculated OH reactivity (left) and the difference between observed and modeled OH reactivity (right). The model-calculated OH reactivity was determined for ambient conditions (no-het) and for the OHR flow tube pressure and temperature (tube p&T). See text for explanation. Dotted vertical black lines on right are approximate indicators of measurement-model agreement.
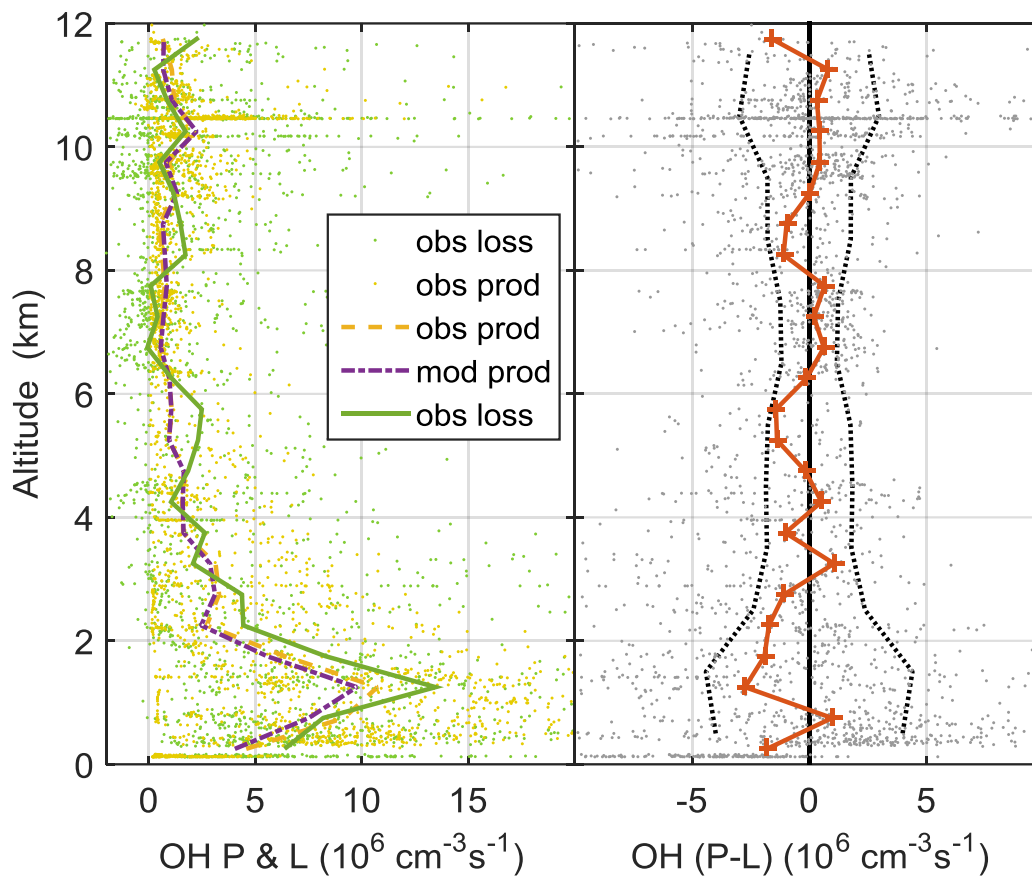
Figure 6. OH production and loss (left) and difference between measured OH production and measured OH loss, cm[-3]s[-1] divided by 10[6] (right). Modeled OH production and loss are equal. Dots are individual one-minute calculations of OH production using observed atmospheric constituents and photolysis frequencies. Dotted vertical black lines on right are indicators of OH production and loss agreement at the 1σ confidence and were determined by a propagation of error analysis.
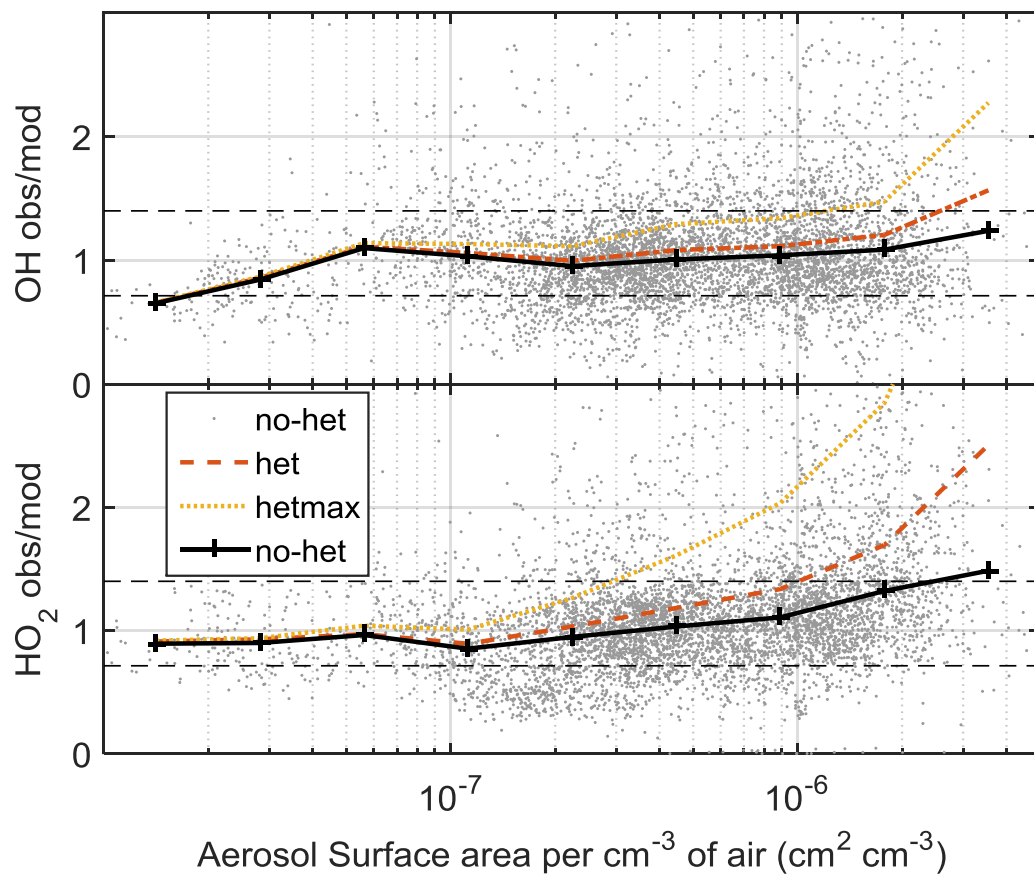
Figure 7. Median observed-to-modeled OH (top) and HO₂ (bottom) versus aerosol surface area per cm-3 of air. Dotted horizontal black lines are indicators of OH production and loss agreement.
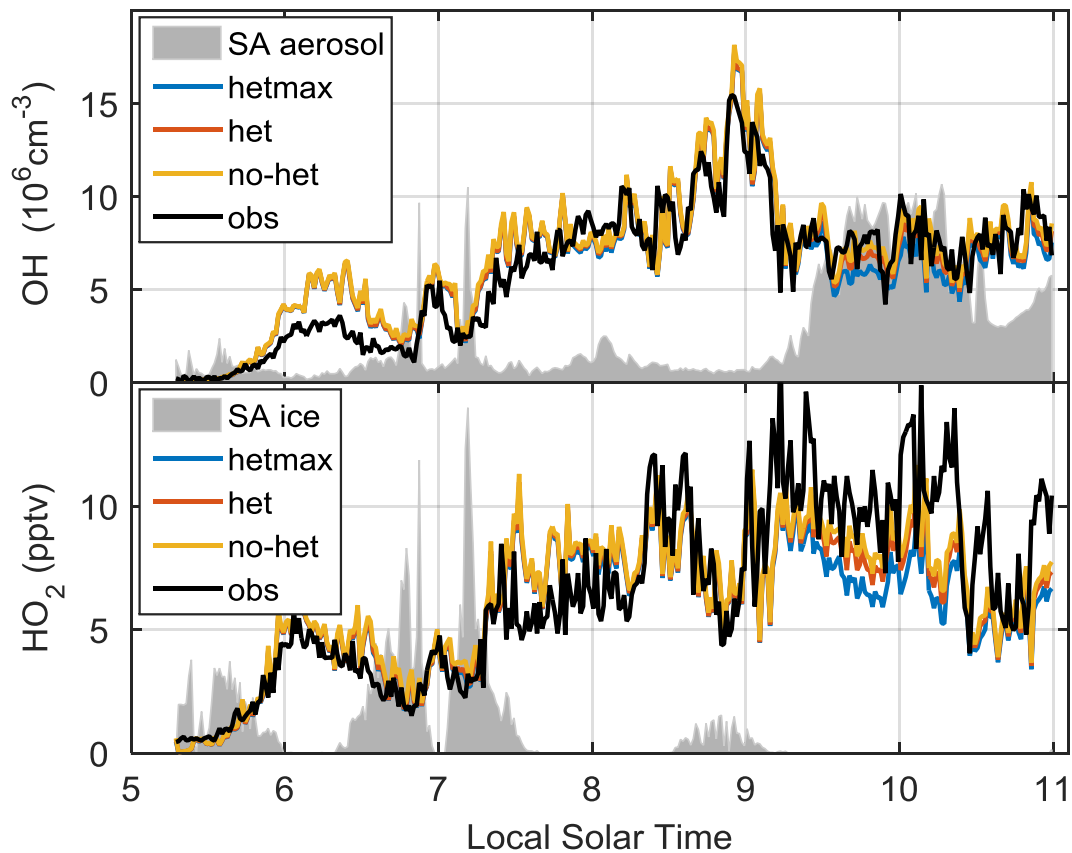
Figure 8. Evolution of OH (top) and HO₂ (bottom) downwind of a MCS. The het and hetmax models are essentially identical to the no-het model for this flight except in heavy aerosol from 9 am to 11 am. The gray shading is scaled aerosol surface area (top panel) and is scaled ice surface area (bottom panel).
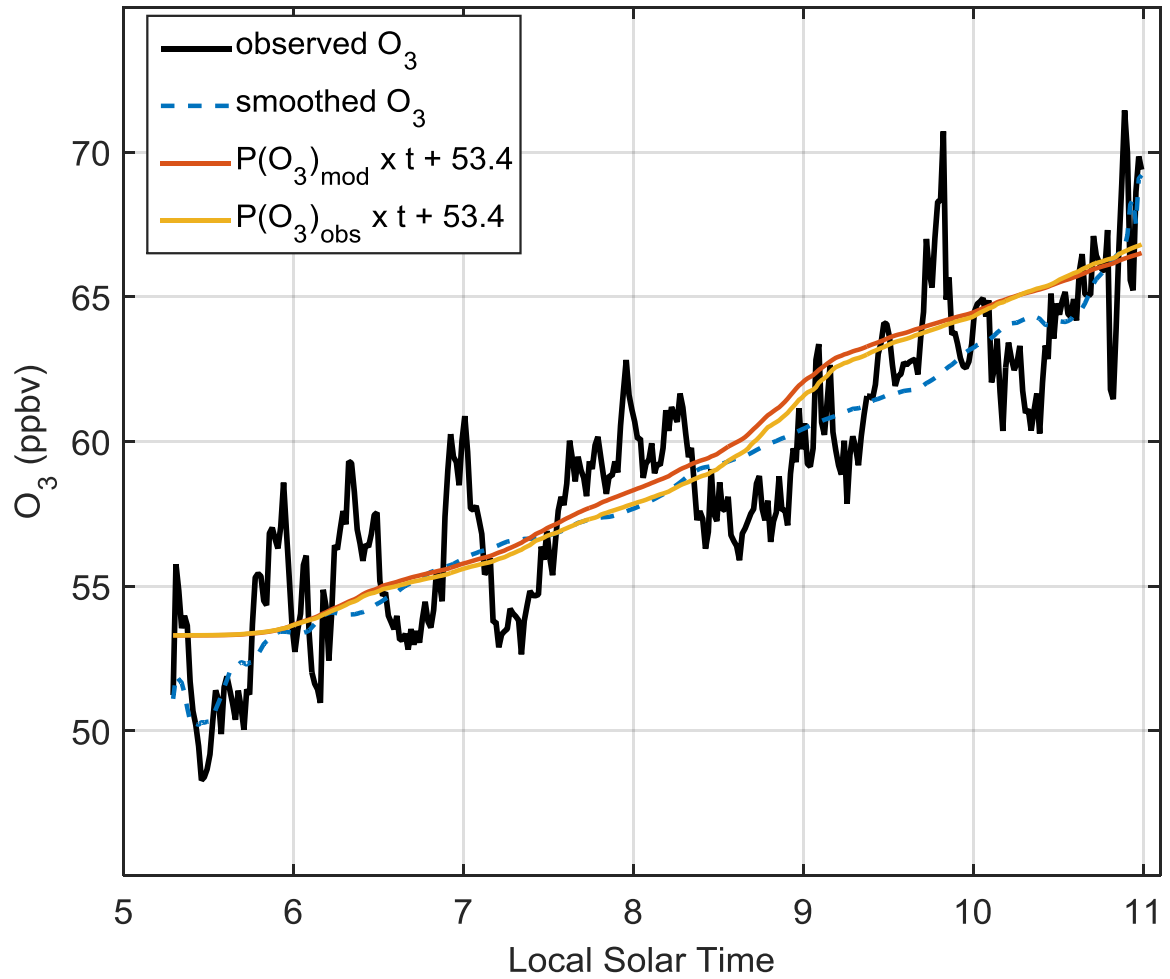
Figure 9. The O_3 trend in MCS outflow. Observed O_3 - one-minute data (black line) and smoothed data (dashed blue line, 180-min filter) - show variability along the legs set perpendicular to the air flow and also show the O_3 trend with time. The calculated O_3 uses the accumulated calculated O_3 production rates ($P(O_3)$ x time) for observed (yellow) and modeled HO_2 (red) and adds those values to an initial value of 53.4 ppbv to show the calculated O_3 trend.

Table 1. Measured chemical species

Chemical species	Accuracy (2σ confidence)	Time resolution	Reference that describes the instrument
OH, HO$_2$	±32%	20 s	Faloona et al., 2004
NO; NO$_2$; O$_3$	0.01 ppbv + 4%; 0.02 ppbv + 6%; 0.04 ppbv + 3%	1 s	Ryerson et al., 2000; Pollack et al., 2011
HCHO	±10% + ±10 pptv offset	1 s	Cazorla et al., 2015.
NO$_2$; PNs; MPN, ANs	±5%; ±10%; ±15%;	15 s	Thornton et al., 2000; Day et al., 2002
CO, CH$_4$, N$_2$O	±2% or 2 ppbv	1 s	Sachse et al., 1991
SO$_2$; HCl; PAN, PPN, HNO$_4$	±15% ±20% ±30%	10 s	Huey, 2007
H$_2$O$_2$, CH$_3$OOH, ISOPOOH, Glycolaldehyde, IEPOX, C$_5$H$_{10}$O$_3$, C$_5$H$_8$O$_3$, Ethanal_Nitrate, Hydroxyacetone, Hydrogen cyanide, HNO$_3$, Isoprene Nitrate, Peroxyacedic Acid, Propanone Nitrate	±(40-80)% ±50% + (25-100) pptv offset	10 s	Crounse et al., 2006
Isoprene, Monotepenes, MVK/MACR, Acetone/Propanal, Methanol, Acetaldehyde, Acetonitrile	±10%	2 s	Mielke, et al., 2008
Ethyne, Ethane, Ethane, Propene, Propane, i-Butane, n-Butane, i-Pentane, n-Pentane, n-Hexane, n-Heptane, 2,3-Dimethylbutane, 2-Methylhexane, 3-Methylhexane, Cyclohexane, Benzene, Toluene, m,p-Xylene, o-Xylene, Ethylbenzene, cis-2-Butene, trans-2-Butene, C8-Aromatics/Benzaldehyde, DMS, Methyl nitrate, Isoprene, α-Pinene, β-Pinene, several halogen-containing compounds	±10%	Variable, seconds to minutes	Colman et al., 2001
H$_2$O	±5% or 1 ppmv	1 s	Vay et al., 1998

Table 2. Scatter plot statistics for OH and HO_2

case	molecule	units	slope	intercept	R^2	ratio
no-het	OH	10^6 cm^{-3}	1.00	0.01	0.85	1.03
	HO_2	pptv	1.00	0.36	0.68	1.10
het	OH	10^6 cm^{-3}	1.07	0.02	0.87	1.11
	HO_2	pptv	1.14	0.51	0.62	1.28
hetmax	OH	10^6 cm^{-3}	1.24	0.03	0.85	1.29
	HO_2	pptv	1.53	0.68	0.50	1.83